Muon Veto Study Comparing pDOM and mDOM for IceCube-Gen2

Bachelorarbeit aus der Physik

vorgelegt von
Julian Saffer
27. September 2017

Erlangen Centre for Astroparticle Physics
Friedrich-Alexander-Universität Erlangen-Nürnberg

Betreuer: Prof Dr. Gisela Anton
Dr. Thorsten Glüsenkamp

Abstract

The extension of the IceCube South Pole Neutrino Observatory, namely IceCube-Gen2, is currently being planned. Hereby, various detector geometries and DOM designs have been proposed so far. The registration of down-going cosmic ray induced muons is an important aspect of neutrino detection in order to suppress the atmospheric background. Therefore, outer layers of the detector array are used as a veto. The pDOM and mDOM are compared in terms of their veto potential using the Sunflower-240m geometry. For that purpose down-going muons following an E^{-3} and $E^{-1.5}$ spectrum for 100 GeV$< E_\mu <$1 PeV are produced in Monte Carlo simulations. Another $E^{-1.4}$ dataset in the range 3 TeV to 100 PeV is used for some parts of the analysis as well. Using the segmented mDOM generally yields a higher veto efficiency. It further increases with E_μ and is maximal for muons with a zenith angle close to 0. The best veto definition occupies 15 top DOM layers.

Zusammenfassung

Die Erweiterung des IceCube-Südpol-Neutrino-Observatoriums ist zur Zeit in Planung. Dabei wurden bereits viele verschiedene Detektorgeometrien und Designs neuer DOMs vorgestellt. Die Erkennung von Myonen, die durch kosmische Strahlung erzeugt werden, ist ein wichtiger Bestandteil der Neutrino-Detektion, um den atmosphärischen Hintergrund zu unterdrücken. Hierfür werden äußere Schichten des Detektors als Veto benutzt. Der pDOM und mDOM werden hinsichtlich ihres Veto-Potentials in der Sunflower-240m-Geometrie verglichen. Zu diesem Zweck werden nach unten propagierende Myonen, welche einem E^{-3}- und $E^{-1.5}$-Spektrum folgen, für Energien 100 GeV$< E_\mu <$1 PeV in Monte-Carlo-Simulationen erzeugt. Für einige Teile der Analyse wird zudem ein weiterer $E^{-1.4}$-Datensatz im Bereich 3 TeV bis 100 PeV verwendet. Mit dem segmentierten mDOM wird allgemein eine höhere Veto-Effizienz erreicht. Diese nimmt mit E_μ weiter zu und ist maximal für Myonen aus dem Zenit. Die beste Veto-Definition belegt die 15 obersten DOM-Schichten.

Contents

1. Introduction

In recent decades new areas of astronomy have developed along with the detection of radiation in more and more energy regimes of the electromagnetic spectrum ranging from radio to gamma rays. In particular the field of high-energy neutrino astronomy emerged as the first neutrino telescopes like BAIKAL, ANTARES and AMANDA were built in the 90s and the beginning 21st century.

Neutrinos are valuable messenger particles since they only interact weakly with matter. Therefore, they hardly get absorbed by cosmic gas and dust clouds or massive bodies like stars and planets. They are also not deflected by magnetic fields. Hence, neutrinos can easily reach Earth directly from cosmic distances. This gives a certain advantage over photons and cosmic rays, which have a cosmologically small range or do not allow simple source reconstruction due to their prior magnetic deflection, respectively.
This strong penetration power in return makes the observation of neutrinos extremely challenging, as they hardly interact with any detector material, too. Due to the small neutrino-nucleus cross-section, a Cherenkov detector with huge instrumented volume is required to ensure a sufficient interaction rate for the indirect detection of cosmic neutrinos. IceCube is such a cubic-kilometer Cherenkov telescope using the Antarctic ice as detector medium.

The major background for neutrino detection in IceCube is the production of muons via the interaction of cosmic rays in the Earth's atmosphere. These muons have to be exposed as atmospheric muons entering the detector as they otherwise might fake neutrino induced muons. For this purpose, an active muon veto can be defined to spot incoming atmospheric muons.

Within the current planning of the detector upgrade 'IceCube-Gen2', several ideas of optical module (DOM) and detector geometries have been developed. In this thesis, the veto efficiency of the mDOM module will be compared against the pDOM in terms of energetic and angular dependencies. Each time the DOMs are deployed in the proposed Sunflower-240m geometry, bordering IceCube. Therefore, possible veto regions as well as strategies will be defined to identify atmospheric muons entering the detector. For this purpose, Monte Carlo simulations of down-going muons in the range 100 Gev $< E_\mu <$ 1 PeV will be performed.

The production of high-energy neutrinos in space and their detection by means of the Cherenkov effect are approached in chapter 2. In the third part the current design of the IceCube Observatory is presented along with the planned Gen2 extensions. Hereby, special features of the proposed DOM designs and detector geometries are discussed. Subsequently, chapter 4 introduces the HESE and muon veto techniques. In this context veto regions and strategies are defined for later examination. The Monte Carlo simulation and treatment of muon datasets for the subsequent analysis are explained in section 5. All analytical results are summarized in the sixth part. After testing the compatibility of

all datasets, both optical modules are compared, using the realistic designs. Dependencies on veto region, strategy and direction are investigated and the veto efficiency is attempted to be extrapolated beyond the simulated energy range. The required number of veto hits is varied to check its impact on the veto efficiency. Lastly, a short analysis using equalized quantum efficiencies is conducted. Final conclusions eventually are drawn in chapter 7, along with an outlook.

2. High-Energy Neutrino Astronomy with Cherenkov Telescopes

High-energetic neutrinos ($E_\nu > 1$ GeV) are special messenger particles with the potential to provide information about several astrophysical objects. Neutrinos have no electrical charge and negligible mass, so they essentially only interact weakly with matter. Therefore, they leave their production site practically without any disturbance and propagate through space with velocities close to the speed of light. This is the reason, why for cosmological distances neutrinos have certain advantages over high-energetic photons which are likely to get absorbed by dust and radiation fields like the cosmic microwave background (CMB), and charged cosmic rays (CRs) which get deflected by magnetic fields.

High-energy neutrinos are a frequent by-product of relativistic CRs interacting with interstellar medium and radiation fields and can therefore be used as unambiguous evidence of hadron acceleration. Those CRs, in the first place, have their origin in Galactic as well as extragalactic sources. The major portion of CRs produced in the Galaxy is provided by heavy charged nuclei and mainly protons. Those are accelerated on the shock fronts of supernova remnants as well as relativistic particles ejected in the jets of microquasars and pulsars. Their energy is constrained by $10^{17} - 10^{18.5}$ eV. Even higher-energetic particles would easily escape the Milky Way, surpassing the influence of the Galactic magnetic field before they could reach the Earth. The CR flux beyond EeV energies consequently is dominated by extragalactic sources. Those are mainly thought to be active galactic nuclei and gamma ray bursts ejecting highly relativistic particles into space [24].
Cosmic neutrinos are a fundamental key for the understanding of the acceleration processes of hadrons. They are providing complementary information in the frame of multi-messenger astronomy besides photon, cosmic ray and, since recently, gravitational wave astronomy.

2.1. Production of Astrophysical Neutrinos

High-energetic CRs can collide with matter or radiation fields (like the CMB) while propagating through space. This leads to the production of pions

$$\mathrm{p} + \mathrm{N} \rightarrow \pi + \mathrm{X} \tag{2.1}$$

$$\mathrm{p} + \gamma \rightarrow \Delta^+ \rightarrow \begin{cases} \pi^0 + \mathrm{p} \\ \pi^+ + \mathrm{n} \end{cases} \tag{2.2}$$

where π can be charged or neutral pions, N is a nucleus and X is an unspecified hadronic remnant. Reaction (2.1) is called a hadronuclear interaction while (2.2) is known as the photohadronic channel. Neutral pions generally decay into two gamma photons, positively charged pions decay preferably into anti-muons

$$\pi^+ \rightarrow \mu^+ + \nu_\mu$$

which subsequently decay into positrons

$$\mu^+ \rightarrow \mathrm{e}^+ + \bar{\nu}_\mu + \nu_\mathrm{e}$$

eventually leading to a flavor ratio of neutrinos $\left(\overset{(-)}{\nu}_\mathrm{e} : \overset{(-)}{\nu}_\mu : \overset{(-)}{\nu}_\tau\right) = (1:2:0)$, which is a certain scenario that is often discussed. This ratio, however, equates to $(1:1:1)$ at Earth due to neutrino oscillations after a long propagation length [24, 31]. This is the reason why all neutrino flavors are relevant to detect in order to learn about the processes taking place in the sources. The decay of neutrons produced in (2.2) for example contribute to one beside many scenarios influencing the original flavor ratio.

2.2. Interaction of Neutrinos with Matter

Due to the small neutrino-nucleon cross-section [31]

$$\sigma \approx \frac{E_\nu}{\mathrm{GeV}} \cdot 10^{-38}\ \mathrm{cm}^2 \tag{2.3}$$

the interaction of neutrinos with matter is a very rare event. Overall, there are the two possibilities of charged current (CC) and neutral current (NC) interaction. In the NC channel, a neutrino scatters off a nucleus via exchange of a Z^0 boson elastically

$$\nu_\mathrm{x} + \mathrm{N} \rightarrow \nu_\mathrm{x} + \mathrm{N}$$

or deep-inelastically

$$\nu_\mathrm{x} + \mathrm{N} \rightarrow \nu_\mathrm{x} + \mathrm{HS}$$

where HS denotes a hadronic shower. All three flavors ($\mathrm{x} \in [\mathrm{e}, \mu, \tau]$) contribute equally to this channel.
In addition, there is one important interaction process specific for electron antineutrinos. With an energy $E_\nu = 6.3$ PeV, electron antineutrinos can scatter off electrons resonantly, creating an on-shell W^- boson (Glashow resonance)

$$\bar{\nu}_\mathrm{e} + \mathrm{e}^- \rightarrow \mathrm{W}^- \rightarrow \ldots$$

which subsequently decays into leptons or hadrons [14].
Also in the CC channel, a neutrino can decay to its corresponding charged lepton, conserving the flavor by exchanging a W boson with a nucleus:

$$\nu_\mathrm{x} + \mathrm{N} \rightarrow \mathrm{x}^- + \mathrm{HS} \tag{2.4}$$

With increasing energy, the angle between the neutrino's and the secondary lepton's direction decreases, allowing the reconstruction of the neutrino's direction by observing the lepton propagating through the detector. Process (2.4) is possible for all three flavors, however, their event signatures in the detector differ from each other significantly. In ice, electrons quickly initiate an electromagnetic cascade after they propagated a few centimeters, overlaying the hadronic shower. Muons, in contrast, have a comparatively long mean free path of several meters up to kilometers before they decay to electrons. So they can be identified by a single long track. Taus, eventually, have the unique feature that they decay hadronically or leptonically (into muons or electrons) after an energy-dependent distance ($\sim 50\ \mathrm{m} \cdot \left(\frac{E}{\mathrm{PeV}}\right)$ [8]). With a DOM (**D**igital **O**ptical **M**odule) spacing dense enough, both showers of an cascade event can be resolved separately ('double bang').

Due to its particularly distinct signature allowing a precise neutrino source reconstruction, the CC muon channel

$$\nu_\mu + \mathrm{N} \rightarrow \mu^- + \mathrm{HS}$$

is often called the 'Golden Channel' of neutrino astronomy despite the limited energy resolution compared to the electron channel. Owing to the long propagation length of high-energetic muons, parts of the track often continue outside the detector. Electromagnetic cascades, however, are concentrated on a smaller volume, well-suited for calorimetric measurements [30].

2.3. Principle of Detection: the Cherenkov Effect

The underlying physical phenomenon used for the detection of particles in neutrino telescopes is the Cherenkov effect. Neutrinos cannot be *seen* as they do not interact electromagnetically and hence can neither emit nor scatter photons at all. Therefore, they only can be detected indirectly by their interaction products.
Charged particles like the leptons created by CC interaction of high-energetic neutrinos with matter (2.4) can exceed the speed of light in this particular medium. Analogous to the Mach cone of a supersonic aircraft, a particle propagating with a velocity $v > \mathrm{c}' = \frac{\mathrm{c}}{n}$ through a dielectric material with an index of refraction n emits so-called Cherenkov radiation in a cone shape with opening angle $\theta_\mathrm{C} = \arccos\left((n\beta)^{-1}\right)$ where $\beta = \frac{v}{\mathrm{c}}$ (see Fig. 2.1). The particle has to have enough kinetic energy to enable this emission process. The energy threshold for the Cherenkov effect evolves as

$$E_{\mathrm{kin,thr}} = m\mathrm{c}^2 \left(\frac{1}{\sqrt{1-n^{-2}}} - 1\right)$$

where m is the particle's rest mass. For a muon in ice ($n \approx 1.33$ [28], thus $\theta_\mathrm{C} = 41.2°$) this results in $E_{\mathrm{kin,thr}} = 54.6$ MeV, i.e. a muon propagating through IceCube losing energy via ionization, bremsstrahlung, pair-production and nuclear interaction will emit

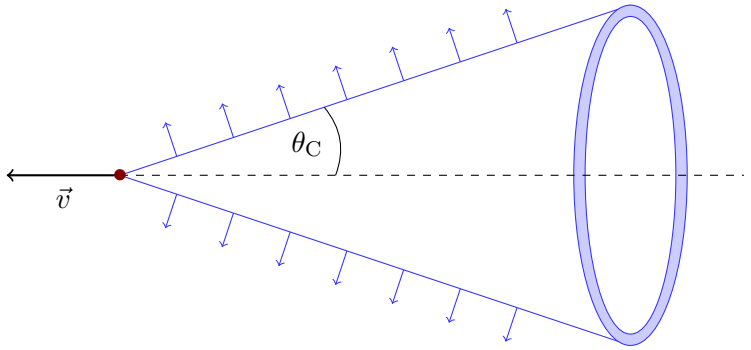

Figure 2.1: A charged particle with velocity $|\vec{v}| > c'$ in a dielectric medium emits Cherenkov light in a cone with opening angle θ_C.

Cherenkov light until its kinetic energy drops below 54 MeV (160 MeV total energy). The Cherenkov spectrum mainly ranges from ultraviolet to blue optical light. In this wavelength regime the emission is proportional to λ^{-2} [24].
The processes leading to muons losing energy primarily can be divided into two types: the almost constant contribution of ionization and the energy dependent radiative (or stochastic) processes composed of bremsstrahlung, pair production and nuclear interaction which roughly scale with E_μ. The energy loss therefore can approximately be parametrized as $-\frac{dE}{dx} = a + bE$. Thus, for low energy ionization dominates, whereas the stochastic processes take over above some critical energy $E_c = \frac{a}{b}$, leading to more radiative emission with increasing energy. Solving this linear differential equation results in $E(E_0, x) = -\frac{a}{b} + \left(E_0 + \frac{a}{b}\right) e^{-bx}$, hence, on a distance $\tilde{x}$ a muon with initial energy E_0 loses

$$\Delta E(E_0, \tilde{x}) = \left(E_0 + \frac{a}{b}\right) \cdot \left(1 - e^{-b\tilde{x}}\right). \tag{2.5}$$

3. The IceCube South Pole Neutrino Observatory

Encompassing a cubic kilometer of ice (1 Gigaton), the *IceCube South Pole Neutrino Observatory* is succeeding the pioneer in-ice Cherenkov telescope AMANDA[1] and is currently by far the largest neutrino telescope in operation. At the geographic South Pole deep in the Antarctic glacier below the Amundsen-Scott South Pole Station IceCube is constituted of an array of Digital Optical Modules detecting Cherenkov light propagating through the highly transparent ice. Indeed, there is no other material known as transparent as the deep Antarctic ice that could be synthesized in that huge amount. Furthermore, background noise from radioactive decay (particularly the β decay of ^{40}K) is highly suppressed compared e.g. to sea water Cherenkov telescopes like BAIKAL and KM3NeT[2].

IceCube also comprises the surface component *IceTop*. Above the in-ice array there are 162 ice tanks deployed, each equipped with two DOMs detecting Extensive Air Showers initiated by cosmic rays in the upper atmosphere. IceTop allows studying the spectrum and chemical composition of the CR flux but can also act as a veto against down-going[3] atmospheric muons, detecting coincident events on the surface and down in IceCube (cf. section 4.2) [3].

With its completion in late 2010, the presently running version *IC-86* (containing 86 strings) started detection leading to the very first observation of a cosmic high-energy neutrino flux [6, 7].
Motivated by this discovery, the potential extension IceCube-*Gen2* is being discussed for the purpose of identifying the high-energy neutrinos' sources by extending the observable energy range beyond EeV energies where the neutrino flux is expected to be extremely low. Therefore, the detector volume has to be increased significantly and new optical modules have to be developed in order to detect more neutrino events.

3.1. IC-86

The current configuration of IceCube consists of 78 vertical strings arranged in an almost hexagonal pattern with a spacing of approximately 125 m and eight additional strings deployed closer together in the center of the array with only ∼70 m spacing (*DeepCore*). Each of those 86 strings holds 60 DOMs with 13 inch diameter [16] connected by cable adding up to 5 160 DOMs in total. Vertically, the DOMs are frozen into position between 1 450 and 2 450 m below the surface with a spacing of 17 m. The DeepCore DOMs are separated by only 7 m or 10 m from each other, respectively, 50 below 2 100 m with the

[1] **A**ntarctic **M**uon **A**nd **N**eutrino **D**etector **A**rray
[2] First, situated in Lake Baikal, Russia, latter the **km^3 Ne**utrino **T**elescope currently planned for three locations in the Mediterranean Sea.
[3] Down-going in this work means zenith angles $0° \leq \theta < 90°$, up-going conversely. However, IceTop's veto capability is limited in the zenith range as explained later.

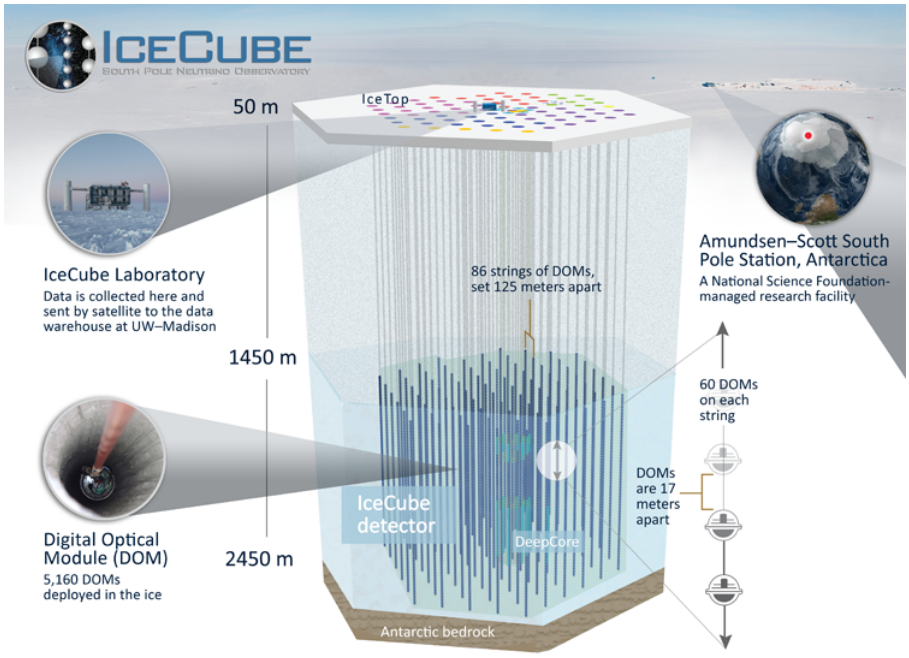

Figure 3.1: The hexagonal detector setup of IC-86, the colors depicted at the surface correspond to the year of string deployment [2].

denser spacing and 10 above 2 000 m where the ice is most transparent[4] (see Fig. 3.1). Due to its dense placement in the IceCube array DeepCore allows to lower the minimum observable neutrino energy from 50-100 GeV [13] to below 10 GeV. This is especially important for researching oscillations of atmospheric neutrinos and the search for dark matter [1].
All signals of detected light are digitized and sent to the surface together with their time information. Events triggered by coincident signals in different DOMs can be reconstructed to obtain the energy from the cumulated charge and the propagation path of the observed particle. For shower events (e and τ) the angular resolution is $\sim 15°$, for tracks (μ) even better than 0.4° [10].

With the recent observation of PeV neutrinos[5] the proof of concept to detect astrophysical high-energy neutrinos has been provided. In order to increase the modest rate of high-energy observations and improve the event reconstruction, an extension of IceCube along with the development of enhanced instrumentation is being investigated.

[4] Between 2 000 m and 2 100 m below the surface there is a layer of dust which increases absorption and scattering of photons significantly [13].
[5] 54 events with deposited energy ranging from 20 to 2000 TeV have been observed [9, 26].

3.2. IceCube-Gen2

Extending the detector volume up to $7 - 10$ km^3 will increase the amount of high-energy samples substantially. So with growing statistics the uncertainties in the PeV- to EeV-neutrino spectrum will shrink further. The development of new optical modules could enable higher sensitivity to dimmer events, the determination of the astrophysical neutrino flavor composition and a better directional resolution and therefore can have a positive impact on the search for neutrino point sources. By building such a *High Energy Array* (HEA)[6], the observation of transient sources - ideally accompanied by several multi-messenger observatories worldwide - like, e.g. an emerging supernova, would come within reach as well [15].
The low-energy sub-array is planned to be improved within the Gen2 extension as well. In the course of the extension inside the ice, the surface detector IceTop might get enlarged, too [10, 11].

3.2.1. pDOM and mDOM

There are several DOM models proposed for utilization in the HEA. Beside the WOM (**W**avelength-shifting **O**ptical **M**odule) [22] and the D-Egg (**D**ual optical sensors in an **E**llipsoid **G**lass for **G**en2) [23], there are the *pDOM* and the *mDOM*.

The pDOM (**P**INGU **D**igital **O**ptical **M**odule) is the modernized version of the DOM which is currently used in the IC-86 configuration and which is considered very reliable[7]. Like its predecessor, it is a glass sphere with 13" diameter containing a single ten-inch photomultiplier tube (PMT) facing down (see Fig. 3.2, left). The pDOM is, however, not entirely blind to down-going tracks since back-scattered light is detected as well. The corresponding electronics placed above the photo sensor have seen some improvements leading to faster processing and reduced power consumption. In the course of revising the DOM, its quantum efficiency (QE) also has been enhanced.
A promising alternative to this initial model is the mDOM (**m**ulti-PMT **D**igital **O**ptical **M**odule). Inspired by the design that is since recently used in the water Cherenkov neutrino telescope KM3NeT, the mDOM comprises 24 three-inch PMTs in a 14" glass sphere[8], adding up to a total effective photosensitive area 2.24 times that of the pDOM. This factor condenses the difference in actual PMT surface and QE. Those PMTs are arranged fairly evenly in the vessel to yield a uniform sensitive area for the total solid angle (see Fig. 3.2, right). Owing to the 4π coverage, each module intrinsically yields directional information of an event. Furthermore, due to the segmentation, local coincidence methods can be applied in order so suppress the noise background emerging from the PMT, which usually is not possible in single-PMT modules [27].

[6] For the sake of differentiation in the following, Gen2 will denote the whole in-ice detector including sub-arrays and yet existing parts, whereas the HEA means the main-array extension only.
[7] The survival fraction exceeds 99 % so far [20].
[8] The shape actually deviates slightly from a perfect sphere since a cylindrical extension is added at the equator in order to fit in all 24 PMTs optimally [16].

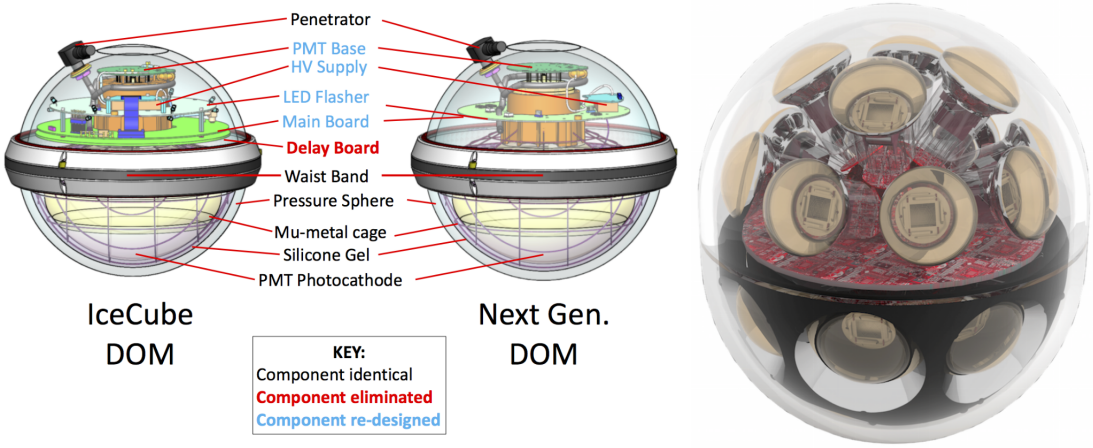

Figure 3.2: *Left:* Improvements of the IceCube DOM towards the Gen2 pDOM [10]. *Right:* Design of the multi-PMT module with 24 smaller optical sensors. For this photo the black holding structure has been removed from the top hemisphere to reveal the interior electronics [25].

	Pro	Contra
pDOM	• very reliable	• low sensitivity to down-going muons • unavoidable noise background
mDOM	• 4π field of view • 2.24× sensitive area • segmentation of sensor	• larger diameter → higher drilling cost • requires more time for development

Table 1: Expected (dis)advantages of pDOM and mDOM, respectively.

Summarizing, the expected advantages and disadvantages of both DOM designs are opposed in Tab. 1.

3.2.2. Detector Geometry of the HEA

In order to search for astrophysical neutrino point sources, the detection of events with energies beyond several PeV has to be facilitated. Due to the low neutrino flux at very high energies, the event rate can be raised by increasing the instrumented detector volume. As previous measurements revealed, the absorption length of Cherenkov photons in the deep Antarctic ice exceeds 100-200 m. Thus, the High Energy Array can be built with much larger string spacing than hitherto used in IC-86, namely increasing the instrumented volume by one order of magnitude while only roughly doubling the number of strings. This raises the energy threshold for observation to few TeV, but does not impair the ability of the HEA to detect high-energetic leptons. For the HEA, several array designs have been proposed, including spacings ranging from 200 m to 300 m, some with just

125 m on the detector edge [10, 15, 18]. For this thesis the so-called *Sunflower* geometry with 240 m spacing is chosen (see Fig. 4.2). The main purpose of this design is to prevent muons from sneaking through the detector (partially) unseen. By using an irregular design, namely a Fermat spiral, exploitation of spacial symmetries and therefore a reduced resolution for track events is avoided. Embedding the IC-86 array, the HEA introduces 122 additional strings, each equipped with 80 DOMs. The detector also grows vertically, as the DOM spacing remains 17 m. Six DOMs are added above and fourteen below the current borders of IceCube, leading to an extension of about 100 m at the top and 240 m at the bottom [10].
Besides the increasing volume the cross-section of Gen2 plays a crucial role for the detection of muons as well. The number of CC ν_e and ν_τ interactions as well as NC events of all flavors scale with the detector volume whereas the chance to observe neutrino induced muons is proportional to the projected area. The 25 % growth in height leads to a significantly increased sensitivity to horizontal tracks. Those provide the best sensitivity for the point-source searches since the range for muon tracks within the detector as well as the projected DOM density are maximal at the horizon [33].

4. HESE Analysis and Muon Veto

Atmospheric muons constitute the main background looking for neutrinos from the Southern sky. A *High Energy Starting Event* (HESE) analysis can be applied for the purpose of excluding those disturbing background tracks. This already has been done e.g. in the recent discovery of cosmic high-energy neutrinos. Hereby, only muon tracks with their starting vertex inside the fiducial volume are considered for the neutrino analysis, whereas entering tracks are vetoed. Therefore, adequate veto regions and strategies are evolved to determine where and how the atmospheric background entering IceCube can be spotted.

4.1. Necessity of Vetoing Muons

Cosmic rays hitting the Earth's atmosphere induce air showers containing among other particles a lot of mesons. Charged pions, for example, decay into (anti)muons and muon (anti)neutrinos

$$\pi^{\pm} \rightarrow \mu^{\pm} + \overset{(-)}{\nu}_{\mu}.$$

While these muons need a minimum energy to reach the underground IceCube array, the neutrinos get there anyway - also from below, created in cascades in the Northern sky. The IC-86 array detects $\mathcal{O}(10^{11})$ of those down-going muons ($\downarrow\mu$) and $\mathcal{O}(10^{5})$ atmospheric neutrinos in one year.[9] In the same time, only about 100 neutrinos originating from astrophysical sources are detected (see Fig. 4.1, left) [5].
One approach to avoid this heavy background of atmospheric muons is to only consider up-going events as those can only be initiated by up-going neutrinos ($\uparrow\nu_{\mu}$), since they are the only particles capable to traverse the Earth, whereas atmospheric muons from the Northern sky are shielded by the Earth. Hereby, one is left with the irreducible background of $\uparrow\nu_{\mathrm{atm}}$ which is difficult to separate from the targeted flux of astrophysical neutrinos [29]. Atmospheric neutrinos can be discarded by applying an energy cut since they obey a softer spectrum than astrophysical neutrinos. Furthermore, consulting Eq. (2.3), the energy-dependent neutrino-nucleon cross-section leads to an absorption of $\uparrow\nu$ at very high energies, so observations are limited there.

In the course of extending the field of view to the Southern sky, reliable methods are needed to recognize $\downarrow\mu$ as atmospheric background. Fortunately, by vetoing $\downarrow\mu$, both charged current and neutral current events initiated by ν_{atm} are revealed as well. In the high energy regime ($>$ PeV) the angle between ν_{μ} and μ created in the meson decay from an atmospheric air shower is usually so small that they diverge from each other by only $\mathcal{O}(m)$ on their way about ten kilometers from the upper atmosphere down to IceCube. Therefore, $\downarrow\nu_{\mathrm{atm}}$ are accompanied by their partner $\downarrow\mu$, allowing to veto atmospheric background events [29].

[9] This corresponds to a trigger rate of ∼3 kHz for $\downarrow\mu$ [15] and ∼ 3 mHz for ν_{atm}.

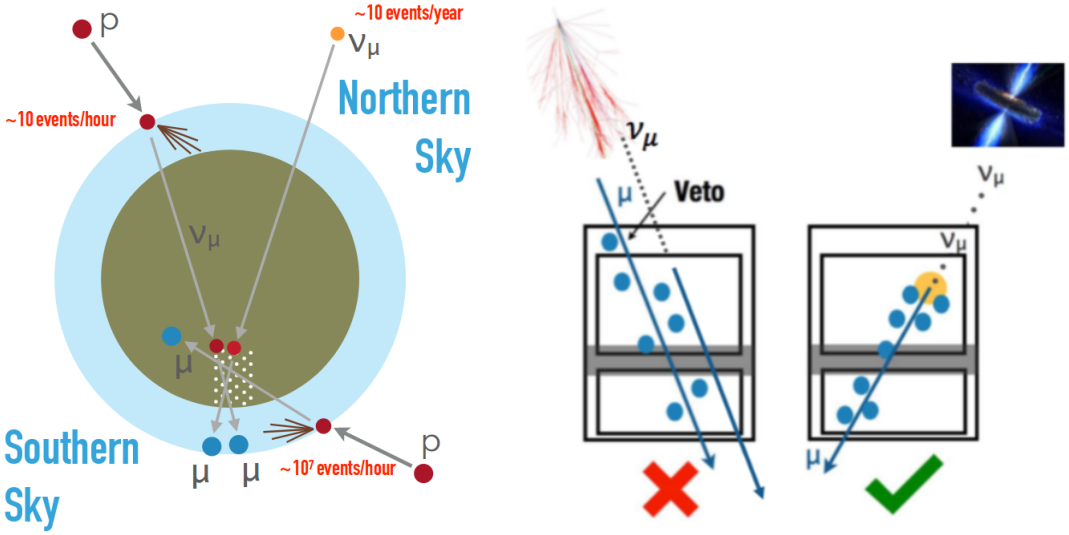

Figure 4.1: *Left:* IceCube (white dots) detects astrophysical neutrinos on top of the heavy atmospheric background from the Northern ($\uparrow\nu_\mu$) and Southern hemisphere ($\downarrow\nu_\mu$ & $\downarrow\mu$) [32]. *Right:* An active veto rejects atmospheric neutrinos since their partner muons can be detected, astrophysical neutrinos, however, initiate starting events with contained vertex [19].

In order to do so, one has to bear in mind that $\downarrow\mu$ entering IceCube are first seen at its edge whereas neutrino induced muons can only be considered when their interaction vertex is contained within the detector volume (starting event). Events that are detected in the outer layers of the detector volume first or are in temporal coincidence with such an event are vetoed and declared as atmospheric background (see Fig. 4.1, right).
As the accompanying muon plays a crucial role in the HESE analysis, its survival is mandatory for an efficient background suppression. A muon needs at least a few hundred GeV to arrive at IceCube, otherwise it is likely to decay $\mu^\pm \rightarrow e^\pm + \overset{(-)}{\nu}_\mu + \overset{(-)}{\nu}_e$, ending up in an electromagnetic cascade, eventually. Thus, the veto efficiency is expected to increase with muon energy (and as a consequence thereof neutrino, meson and CR energy) accessory to the increasing emission of light. Another advantage for vetoing atmospheric muons with higher energy is the shrinking angle between $\downarrow\mu$ and $\downarrow\nu_\mu$ guarantying the vicinity of both particles down in the detector.

Some minor effects on the atmospheric muon veto are e.g. the decay of charmed mesons which decay in more than two products lowering the required neutrino energy for the muon detection. For the decay of unflavored and strange mesons the relation between neutrino and muon energy is given by

$$E_\mu \geq \left(\frac{r_\mathrm{i}}{1-r_\mathrm{i}}\right) \cdot E_\nu$$

where r_i is the mass-square-ratio $(m_\mu/m_\mathrm{i})^2$ with i the parent meson $\pi^\pm$ or $\mathrm{K}^\pm$ [29]. The consideration of muons not only originating in the exact same meson decay but anywhere in the same comic ray cascade enhances the veto probability further [21].

The HESE analysis, therefore, discards all events which are observed in coincidence with an incoming muon track noticeable by its first detection at the edge or which are themselves spotted as incoming $\downarrow\mu$. The residual starting events are then highly probable to be initiated by cosmic neutrinos.

4.2. Veto Regions

There are two distinct methods to veto atmospheric $\downarrow\mu$, one using the CR detector IceTop on the surface above, the other repurposing outer DOM layers of the in-ice detector as a *veto region*. The remaining inner part of the array is the so-called fiducial volume. One advantage in exploiting IceTop is the massive increase in usable volume since all the ice between the surface and the in-ice array is available for neutrinos to interact and initiate a muon track. Furthermore, all DOMs can be used since none are reserved for constituting a veto region. However, from the viewpoint of the IC-86 array, IceTop only covers about 3 % of the Southern sky [10], thus limiting the zenith angle of vetoable atmospheric neutrinos and muons. Although the upgrade IceTop2 may be extended far beyond the footprint of the HEA, a surface veto will never cover the whole zenith range until the horizon.

In this work, the active in-ice self-veto technique will be applied on the Sunflower-240m geometry by defining designated strings and individual DOMs as a continuous veto region. By following distinct strategies (introduced below in section. 4.3), muons with associated hits in this region are declared as atmospheric background. While deciding on the size of the veto region, one has to balance between the efficiency in vetoing incoming muons and the residual amount of fiducial volume, because with growing veto portion it gets more probable that actually astrophysical neutrino events are mistakenly declared as background.
For the purpose of this study three veto regions extending from one to the other and a special fourth region were defined in order to be compared later:

Label	# vertical layers	# horizontal layers	# DOMs	% of IceCube-Gen2
`1_1`	1	1	3 634	24.4 %
`2_2`	2	2	6 901	46.3 %
`2_3`	2	3	7 003	46.9 %
`1_15`	1	15	5 740	38.5 %

Here vertical layers denote those sets of strings at the edge of the array as they are mapped in bird's-eye perspective in Fig. 4.2. For regions `1_1` and `1_15`, only the first layer is used whereas the other two are upgraded with an additional second layer. The DOMs deployed in vertical layers are supposed to detect muons entering IceCube from the side.

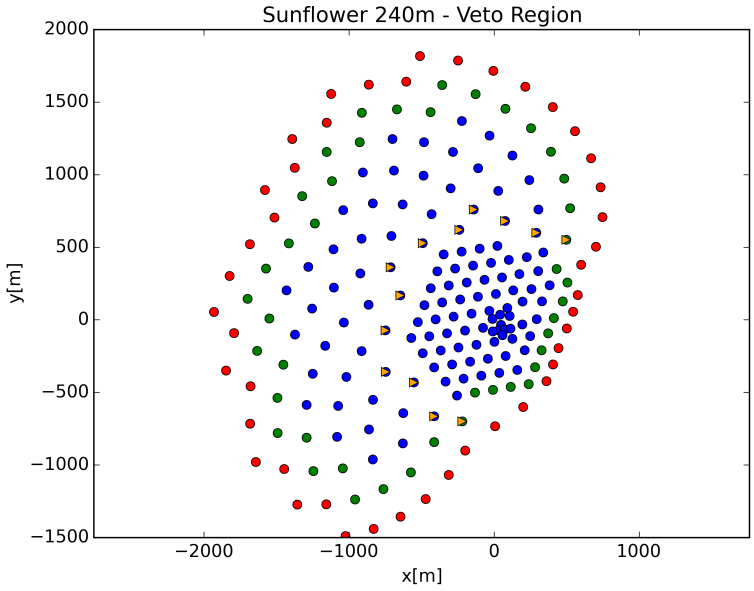

Figure 4.2: First veto layer (red), second veto layer (green), those strings marked with orange triangles only contribute to the veto region in the upper part between the IC-86 cap and the top of the HEA on different levels. For 3-dimensional views of all veto regions see Fig. A.1 - A.4.

In order to catch those hitting the detector cap, the top n ($\in [1, 2, 3]$) DOMs of all strings are defined as part of the veto region as well, constituting the horizontal layers. Since the top edge of the HEA (1 345 m below the surface) is above that of IC-86 (1 450 m) there is a gap of ∼105 m at this step. In order to prevent muons from sneaking through this gap, the DOMs in the top 105 m of the strings at the transition from IC-86 to the HEA (orange triangles in Fig. 4.2) are designated as veto DOMs, too. The DeepCore DOMs do not contribute to any veto region.
Veto region `1_1` occupies almost a quarter of the 14 920 DOMs[10]. This portion nearly doubles considering `2_2` and gets incremented slightly further by 102 additional upper DOMs[11] in the largest region `2_3` (confer [17]). Finally, inspired by the HESE analysis in [12], another veto region is designed containing the upper 15 DOMs of each string providing a much higher sensitivity to incoming particles with small zenith angle. This is especially relevant for the suppression of atmospheric muons since their distribution has its maximum at the zenith ($\theta = 0$). So by bringing the zenith into focus, the separate veto region `1_15` might yield an advantage in vetoing the muon background while occupying significantly less DOMs than those regions comprising two vertical layers. One has to bear in mind, though, that this is not applicable directly to the fraction of occupied detector volume due to the different string geometries in IC-86 and the HEA.

[10] $14920 = 86 \times 60 + 122 \times 80$ (# IC-86 string × # DOMs per IC-86 string + # HEA strings × # DOMs per HEA string).
[11] $102 = 86 + 122 - 44 - 43 - 11 - 8$ (# IC-86 strings + # HEA strings - # strings in 1st layer - # strings in 2nd layer - # strings in step - # DeepCore strings), cf. Fig. 4.2 for color code.

4.3. Veto Strategies

Targeting the identification of *incoming* muon tracks, the temporal evolution of hits has to be considered. Otherwise, particles traversing the veto region while leaving the detector could not be distinguished from those entering it and therefore neutrino induced muons tracking out of IceCube would be declared as atmospheric muons mistakenly. In the context of this study four strategies determining the regarded time interval are defined:

Label	Description
`first_70`	First 70 ns after first hit
`first_140`	First 140 ns after first hit
`first_half`	First temporal half of the event
`ten_first`	Time until 10^{th} hit

The values of 70 ns and 140 ns emerge from the fact that those are about the times a particle moving with the speed of light takes to transit 17 m or 34 m, respectively. This again is the minimum distance between two or three consecutive DOMs. To obtain the first half of an event the midpoint between the moment of the very first hit and that of the last hit is computed. The fourth strategy is based on only considering the ten first hits, no matter which time span they might cover. Needless to say that the ratio between those four distinct terms strongly depends on the temporal distribution of hits, their total number and the duration of the according event. A very short and faint event for instance could be claimed entirely by `first_70`, `first_140` and `ten_first` whereas `first_half` certainly would regard the major portion of a long enduring event with most hits in the middle.
Therefore, it is expected that the `first_half` strategy detects most hits for high energy events but suffers a loss of efficiency with decreasing energy and perhaps even drops below the other strategies at some muon energy value.

5. Monte Carlo Muon Simulation and Dataset Merging

For the purpose of this thesis, both preprocessed muon datasets and new Monte Carlo simulations designed for this study, are integrated. Therefore, one has to test the compatibility between these datasets. Monte Carlo muon simulations are performed with the MuonGun toolkit [4], putting muons in a predefined distance from the detector and simulate their propagation through the ice. Since this study addresses atmospheric muons, only $\downarrow \mu$ were generated. Their zenith angle distribution either corresponds with the actual atmospheric muon flux (sets `20115` & `20134`) or is isotropic over the Southern sky (`12603`) as will be investigated later in section 6.1.1. The desired energy range and spectral index are set in a configuration file beforehand. As the propagating muons are created, their Cherenkov radiation emission and energy losses are simulated afterwards. Eventually, the detection of that light is determined where the QE of the PMT, the effective photosensitive area of the DOMs, and their position as well as spatial orientation are crucial. Noise background in the PMTs is not included in theses simulations.
For each dataset, the exact same set of muons is simulated twice, once with the IceCube-Gen2 detector geometry equipped with pDOMs, the other time with mDOMs. Meanwhile, the modules deployed in IC-86 remain the standard DOMs that stay there unchanged. It should be noted that in dataset `12603` the quantum efficiency of the pDOM has been scaled up artificially by a factor of 2 whereas both new simulations are constituted by one set with realistic DOM sizes and a second with equalized QE (2.24×pDOM). Hereby, the effect of the different sensitive areas is neutralized and only the impact of the DOM geometry is considered.
The starting points of the muons are 50 m (`12603`) and 200 m (`20115` & `20134`) outside an imaginary cylinder encompassing IceCube. This change is done because by doing so, all stochastic energy losses can be considered that produce light even yet outside IceCube but should be seen by the veto DOMs as well. Therefore, the behavior of atmospheric muons is modeled more realistically.

There are some adjustments necessary in order to combine two or more datasets with different simulation parameters. By subtracting the energy loss given by Eq. (2.5) using the parameters $a = 0.24\ \frac{\text{GeV}}{\text{m}}$ and $b = 3.3 \cdot 10^{-4}\ \text{m}^{-1}$ [17], the 150 m gap between the muon sets can roughly be compensated. Also data with deviating spectral indices can be

ID	# events	energy range	γ	θ distribution	μ^- start point	pDOM QE
`12603`	186 000	3 TeV - 100 PeV	1.4	isotropic	50 m outw.	2×
`20115`	100 000	100 GeV - 1 PeV	3	atmospheric	200 m outw.	1× 2.24×
`20134`	65 000	100 GeV - 1 PeV	1.5	atmospheric	200 m outw.	1× 2.24×

Table 2: Simulation parameters of all three Monte Carlo datasets that are used. `20115` and `20134` were produced for this work.

merged by weighting them to be constant (E^0). Therefore, for each energy value in each dataset a corresponding scale factor is computed considering the total number of items per dataset, the spectral indices, the overlap of the energy ranges and the zenith distribution, respectively. Analogous to the energy weighting, with known zenith generation spectrum the zenith angle distributions of the datasets can be adapted to each other. This can be eluded by selecting events out of one zenith bin only.
The important parameters of all datasets used in this work are condensed in Tab. 2.

6. Results

First of all, the comparability of all three datasets is checked by means of their angular distribution, their general DOM hit response and the sensitivity to veto hits in particular. The veto efficiency is compared with the realistic PMT QEs first (with sets `20115` and `20134`). Hereby, the influence of veto region and strategy is investigated as well as the ratio between mDOM and pDOM efficiency. Subsequently, the zenith dependency is analyzed and the veto efficiency is aimed to to be extrapolated to higher energies. A veto definition requiring more than one veto hit is examined as well. In the last part, selected veto combinations are compared once more using the up-scaled pDOM quantum efficiency.

6.1. Consistency of Simulations

In order to demonstrate the compatibility of the new simulated datasets with the older one, first of all, set `12603` is merged with `20115` and `20134`, using the doubled pDOM versions. First contains 83 579 spotted muons. Dataset `20134` (with 39 514 detected muons) is produced additionally to the 47 473 seen muons in set `20115` in order to increase statistics further. In latter, the energy range to 1 PeV is not fully exploited owing to the soft E^{-3} spectrum. The spectra are confronted in Fig. 6.1. At around 1.2 TeV there is a recognizable drop despite the simulation of a second dataset (`20134`).
If not stated otherwise, in this work plotted energy values correspond to the initial Monte Carlo muon energy and, therefore, do not equal the particle's energy during detection after some propagation. The errorbars are estimated with the Poisson standard deviation $\sigma_{\mathrm{P}}(y) = \sqrt{y}$.

6.1.1. Angular Distribution

The distribution of the generated muons with respect to their azimuth and zenith angle is an important property of each dataset. As mentioned before, all muons considered in this work have to be seen with at least one photon for each DOM type. Thus, the observed angular distribution strongly depends on the detector geometry, additionally to the originally preset allocation. In the new simulations, the muons are generated uniformly over the whole azimuth range. The zenith distribution, however, follows the real flux of CR induced muons. Owing to the strong asymmetry of the HEA geometry (cf. Fig. 4.2), the amount of detected muons varies with the azimuth (see Fig. 6.2, left). This applies for all three datasets almost equally.
In contrast to this, the zenith distribution differs significantly from dataset 12603 to the new sets (Fig. 6.2, right). While latter simulations obey the actual flux of atmospheric muons, the older one falls back on an isotropic $\cos(\theta)$ distribution, both convolved with the projected area of IceCube-Gen2. Since the cap surface of the detector is larger than its side view there are more events seen entering from above. This issue might state a critical problem for the comparability of both datasets since the veto efficiency is expected to depend on the zenith angle owing to the different vertical and horizontal spacings.

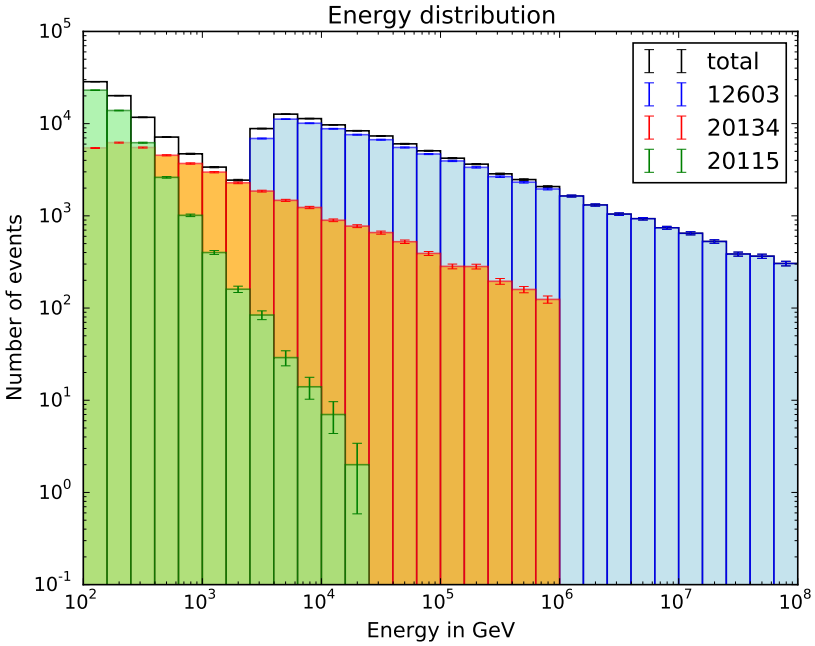

Figure 6.1: Energy spectra of all three datasets. *Blue:* older dataset (ID 12603), *green:* first new set (20115), *orange:* second new set (20134).

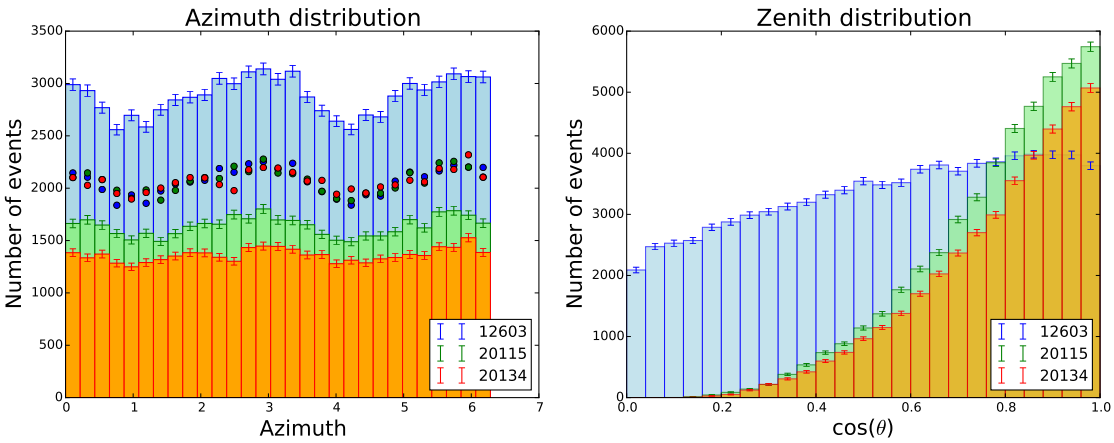

Figure 6.2: *Left:* The azimuthal distribution of detected muons in both datasets. The dots represent the weighting on a same, but arbitrary event number. *Right:* The zenith angle distribution.

This could be solved by weighting the zenith angle just as it has been done for the energy spectrum, in case that the exact generation spectra are known. For simplicity, however, the selected zenith angles also can be constrained on a few zenith bins with $\cos(\theta) \lesssim 1$, since this is the direction of the atmospheric muons of most interest for this background veto analysis, anyway. Although such a cut reduces the effect of deviating zenith distributions for the following analyses, the set of events, hereby, shrinks significantly.

6.1.2. Energy - (Veto) Hit Number Relation

In order to be able to evaluate the consistency of both datasets, the deviating energy losses are adjusted and the spectra are weighted according to section 5. Hereby, the spectral energy weighting is done before the adaption of energy losses. This actually should be processed the other way around, however, it is more complicated to weight an energy spectrum with adjusted lower energy bound.
By looking at the number of muon events in dependency on the muon energy and cumulative number of photon hits detected by the DOMs, the correlation between those two is obtained. This relation is expected to be linear for high energy and is required to be independent on the dataset. In Fig. 6.3 the number of hits per 2-dimensional bin is plotted logarithmically[12] for the mDOM and the up-scaled pDOM using the merged dataset. The reason for the extension to energies below 100 GeV (cf. Tab. 2) is the consideration of energy losses for 150 m in the new datasets. Although an edge is recognizable at approx. 2 TeV due to the loss of statistics in this range and the different QE scalings for the pDOM, the hit response appears to continue quite well from one set to another. The datasets seem to perform consistently, so far.

Since for this study the hit response in the veto is important in particular, next, the amount of events per number of veto hits and energy bin is plotted separately for dataset `12603` and the combined sets `20115` and `20134`. Therefore, the mDOM is chosen, using veto region `1_15` and strategy `first_half`. In order to aim for best comparability between old and new data, here, only those muon tracks are regarded, that penetrate the IceCube-Gen2 array from above and deep in the fiducial volume. Therefore, three cuts are applied on the muon sets: The muon's track length has to exceed 1 600 m, the zenith angle has to obey $\cos(\theta) > 0.95$ and the muon start point has to be at least 300 m inside the Gen2 footprint. So, muons that intersect IceCube at its edge and leave the detector after a few meters ('corner clippers') are excluded. The resulting plots are depicted in Fig. 6.4.
Each vertical strip is normalized to 1, so the color code directly reveals the relative abundance in a certain veto hit bin. By looking at the bottom row, one obtains, how common veto DOMs are *not* hit in the required time interval. As expected, the right plot shows that with increasing energy more frequently at least on veto DOM is triggered. This, however, is just a qualitative observation since the actual ratio can not be read off the '# event' axis due to the energy weighting. On the left side, there are no events hitting no veto DOMs above 10 TeV. In the right plot, there are 'zero-hits' up to ~ 30 PeV despite the lower statistics.

[12] In this work log always denotes the logarithm with base 10.

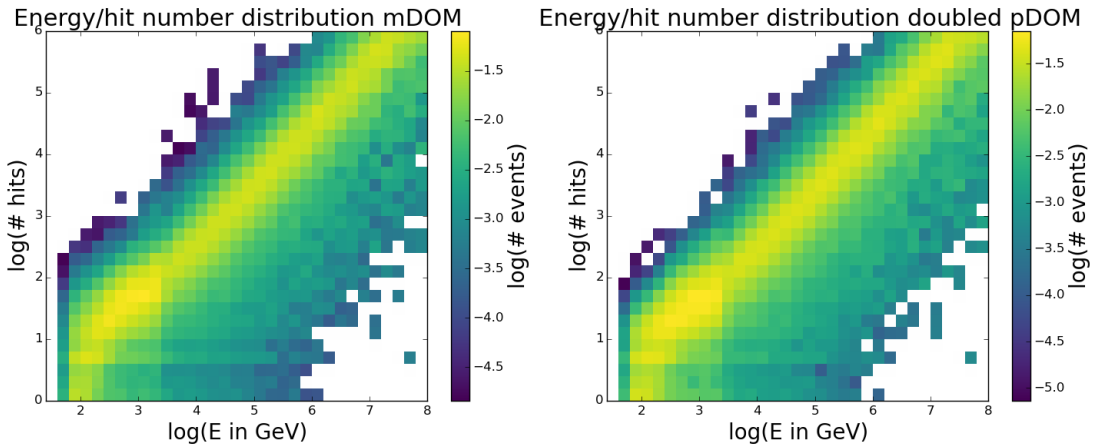

Figure 6.3: *Left:* The number of events over the number of hitting photons and muon energy as seen by the mDOM. *Right:* Same by the pDOM, but at low energy scaled by a factor 2.24, for high energy by 2; the log(# events) scale has arbitrary numbers due to the weighting.

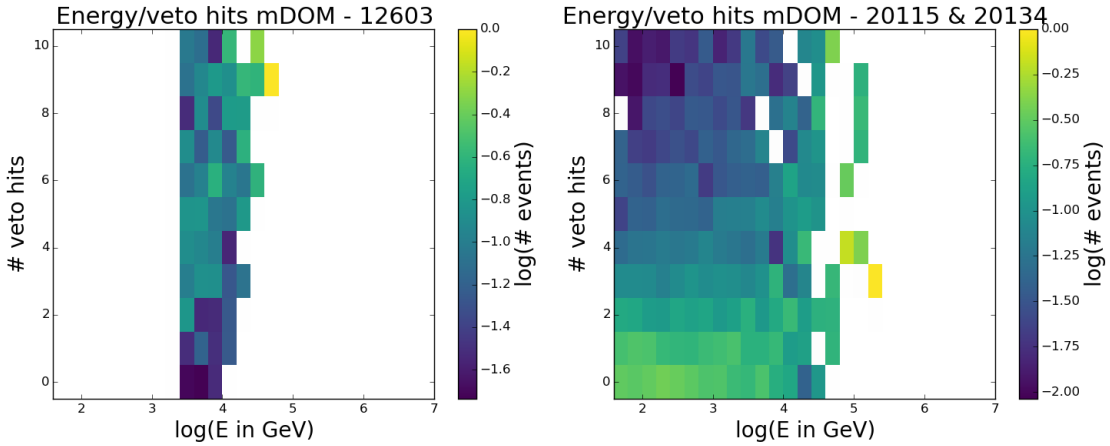

Figure 6.4: *Left:* The number of events over the number of photon hits fulfilling the veto criteria and muon energy in 12603. *Right:* Number of evens over number of photon hits fulfilling the veto criteria and muon energy in 20115 & 20134. In both plots each energy bin is normalized on the vertical axis.

This deviating veto hit response urges to be careful at merging all three datasets for veto analyses.

6.2. Veto Efficiency

For each combination of veto strategy and region it is checked whether the remaining Monte Carlo muons are spotted in the veto successfully or not. The ratio of vetoed muons to the total amount in one bin is the *veto efficiency* η.

In the first simulation (ID `20115`), 100 000 muons are generated allowed in the range 100 GeV to 1 PeV. Owing to the soft E^{-3} spectrum the few most energetic detected muons only have about 20 TeV (cf. Fig. 6.1). Since this results in a significant loss of statistics for TeV energies and only provides a small overlap between the data with the preprocessed set, a second simulation with a much harder $E^{-1.5}$ spectrum is run (`20134`). In this simulation run 65 000 events are obtained.
The following section 6.2.1 considers analyses conducted with the new datasets only. Here the pDOM and mDOM are simulated with their actual quantum efficiency. Subsequently, in section 6.2.2 the respective sets with up-scaled pDOM in combination with dataset `12603` are used. This is conducted in order to examine the exclusive influence of the omnidirectional view of the segmented DOM by disregarding the associated increase in sensitive area.

In order to exclude corner clippers which are not interesting for real analysis, a cut on the muon track length of 1 600 m is applied in chapter 6.2.1. This is combined with a zenith cut at $\cos(\theta) > 0.85$. In section 6.2.2 more strict cuts are applied.
In real event selection, it is common to demand at least $\mathcal{O}(10)$ triggered DOMs ('NChannel') per muon event. This is renounced here, since this would bias low energy events. High-energetic muons generally emit enough Cherenkov light to illuminate more than ten DOMs, whereas this happens quite rarely with $E_\mu \approx 100$ GeV. Therefore, such a NChannel cut would result in an overestimation of the veto efficiency at sub-TeV energies. The length cut, on the other hand, provides a more unbiased sample of through-going tracks.

6.2.1. pDOM/mDOM Comparison Using Realistic Modules

6.2.1.1. Comparison of Veto Regions

As the first veto regions that are defined in section 4.3 are build on one another with increasing volume, it is reasonable to expect an increase in veto efficiency from region `1_1` up to `2_3`. Since `1_15` is especially designed for steeply penetrating muons, this veto region may provide even better results thanks to the major flux originating in the zenith. In order to check this supposition, the energy-binned veto efficiency is plotted for all four veto regions. For this purpose, the strategies `first_70` and `first_half` are chosen

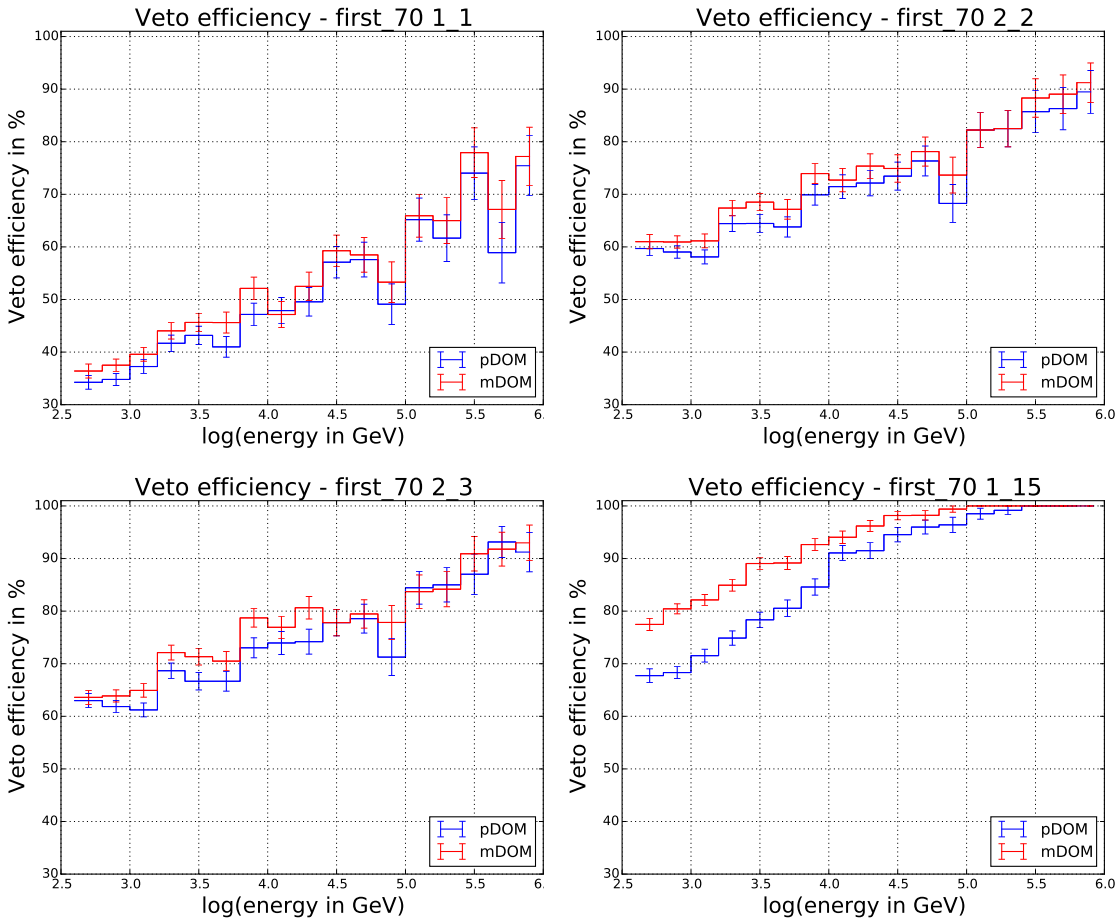

Figure 6.5: Confrontation of the veto efficiencies in all four regions using veto strategy `first_70`.

exemplary (Fig. 6.5 and 6.6). The associated plots for the remaining strategies can be found in the appendix (Fig. A.5 and A.6).
The error on the veto efficiency $\eta_\mathrm{i} = \frac{v_\mathrm{i}}{a_\mathrm{i}}$ is estimated with the binomial error

$$\Delta\eta_\mathrm{i} = \frac{\sqrt{v_\mathrm{i}\,(1-\eta_\mathrm{i})}}{a_\mathrm{i}} \tag{6.1}$$

with a_i the total amount and v_i the vetoed part of muons in the i-th bin.
As expected, the increasing light emission with rising energy leads to higher veto efficiency apart from some fluctuations within the error range. Almost consistently, the veto efficiency of the mDOM exceeds that of the pDOM, as was already suspected by the 4π field of view and about doubled sensitive area. Regions `2_2` and `2_3` only differ slightly from each other by a growth in average of about 3 percentage points for `first_70` and nearly 2 percentage points for `first_half`. Region `1_1` provides the worst η for a given

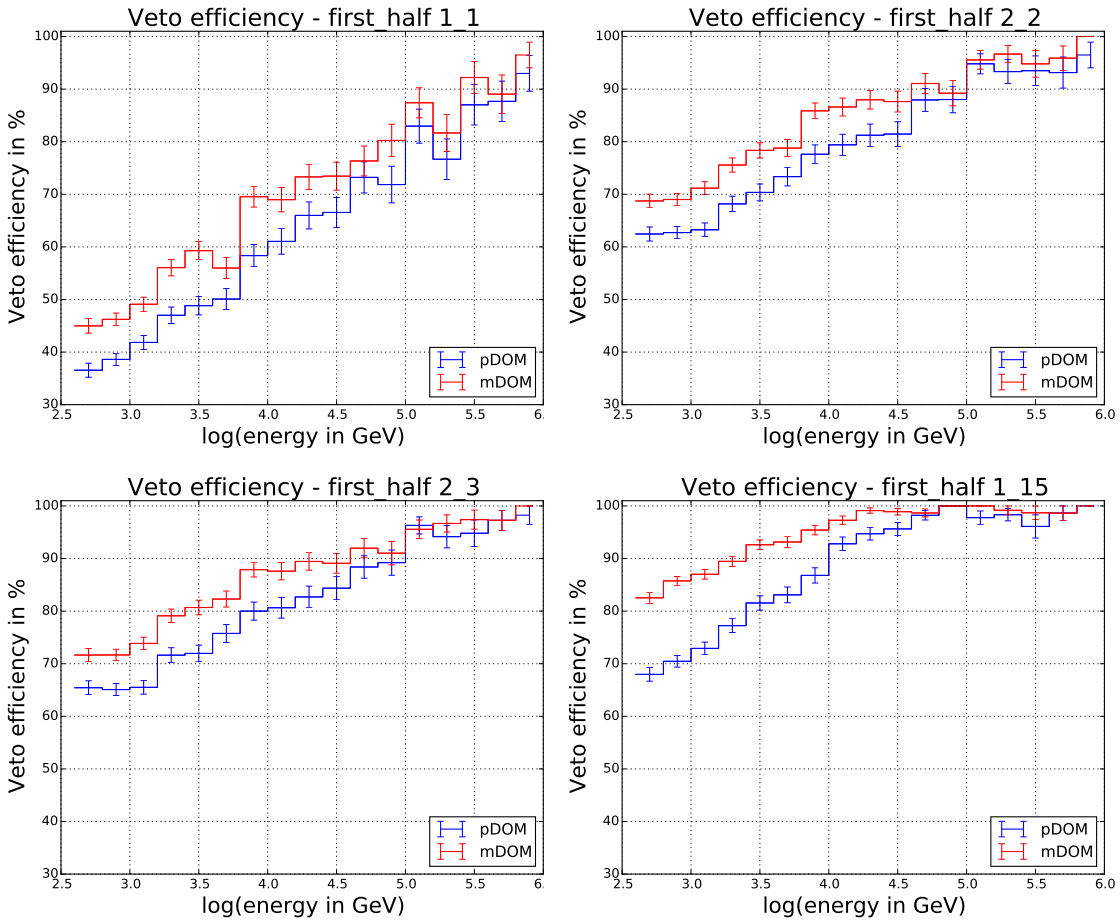

Figure 6.6: Confrontation of the veto efficiencies in all four regions using veto strategy `first_half`.

muon energy, whereas `1_15` vetoes the most incoming muons. Above 100 TeV an efficiency up to 100 % can be achieved, although the binomial error estimate (6.1) for 0 % and 100 % vanishes by definition. This certainly is not a sufficient estimation here, especially, regarding the decrement of events with higher energy. Exemplary, selected values for the veto definitions `first_70/2_2` and `first_half/1_15` are given in Tab. 3.

6.2.1.2. Comparison of Veto Strategies

Vice versa, the effect of the chosen strategy on the veto efficiency is investigated by plotting η over muon energy again, but this time retaining the veto region in order to compare the four strategies. Therefore, region `1_15` is selected, since it exposed as the most efficient veto region in the previous section. For the resulting plots see Fig. 6.7.

η in %	first_70/2_2		first_half/1_15	
	pDOM	mDOM	pDOM	mDOM
$\lesssim 1$ TeV	59.0 ± 1.2	60.9 ± 1.2	70.5 ± 1.2	85.8 ± 0.9
$\gtrsim 10$ TeV	71.5 ± 2.3	72.7 ± 2.3	92.8 ± 1.3	97.3 ± 0.9
$\gtrsim 100$ TeV	82 ± 4	82 ± 4	97.8 ± 1.3	100 ± 0

Table 3: Selected values for η using `first_70/2_2` and `first_half/1_15`.

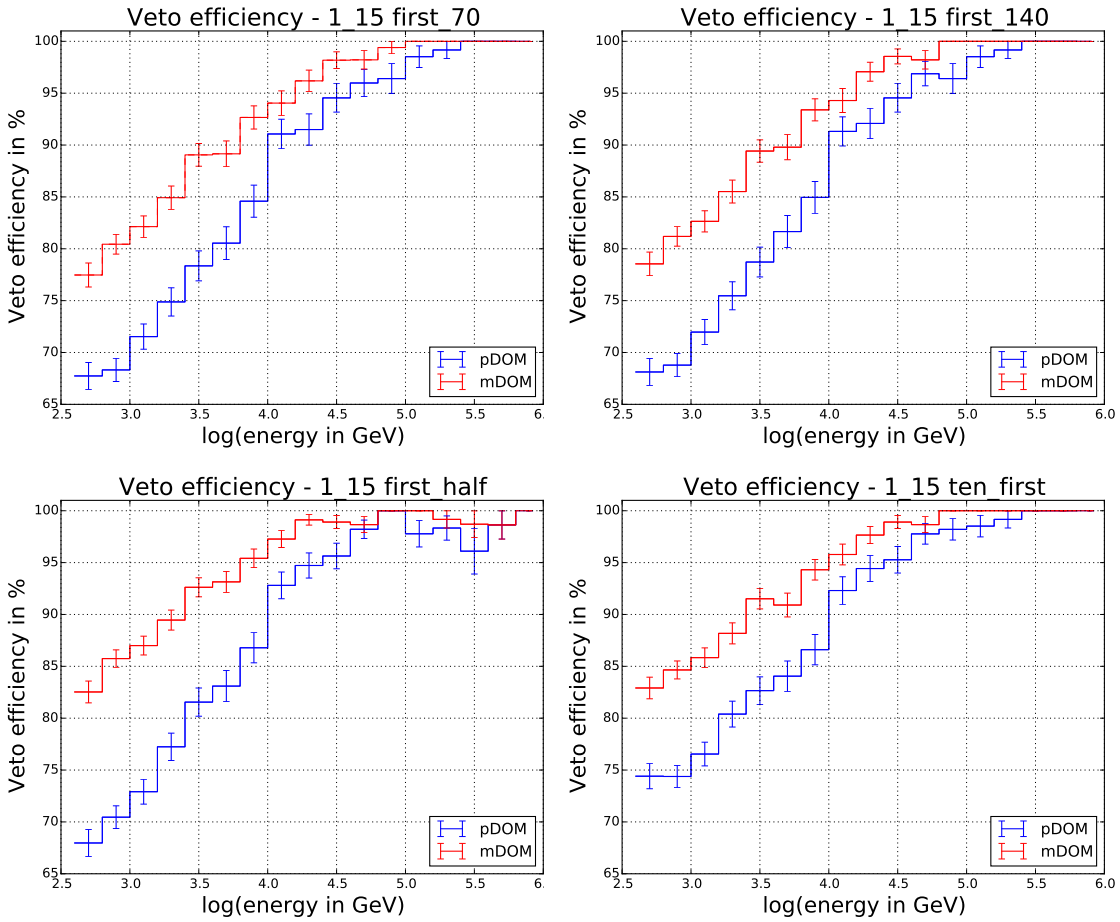

Figure 6.7: Confrontation of the veto efficiencies with all four strategies in veto region `1_15`.

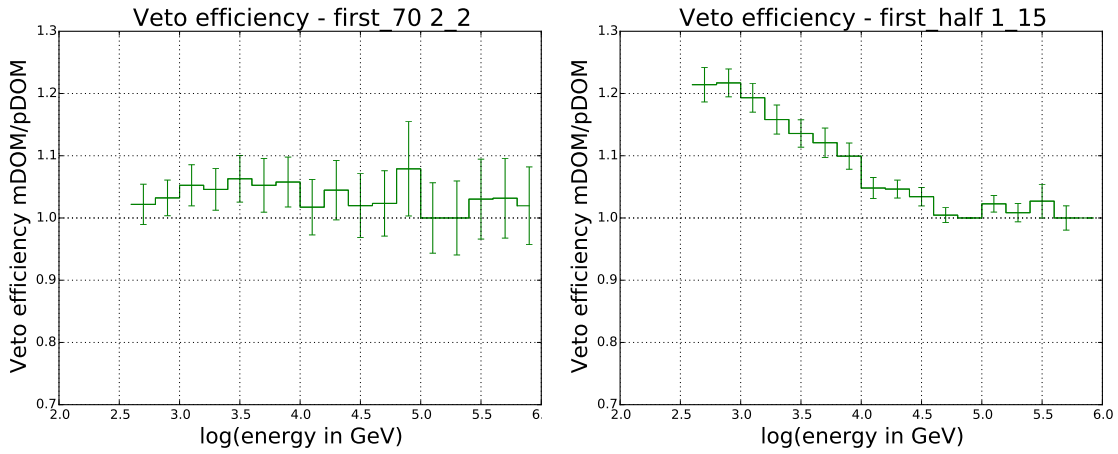

Figure 6.8: The ratio $\frac{\eta_{\mathrm{mDOM}}}{\eta_{\mathrm{pDOM}}}$. *Left:* For the veto definition `first_70/2_2`. *Right:* The veto combination `first_half/1_15`.

All four strategies have in common that $\eta_{\mathrm{mDOM}} > \eta_{\mathrm{pDOM}}$. The largest difference is obtained for low energies with `first_half`. Similar to the comparison of the veto regions `2_2` and `2_3`, the strategies `first_70` and `first_140` follow the same qualitative course, differing by approx. 1-3 percentage points. `first_half` and `ten_first` both achieve higher veto efficiencies. The plots for the remaining veto regions can be found in the appendix (Fig. A.7 - A.9).

6.2.1.3. Veto Efficiency Ratio mDOM/pDOM

When comparing the veto efficiency of the pDOM and the mDOM, not only absolute values, but also their ratio is important. For the combinations `first_half/1_15` and `first_70/2_2` $\frac{\eta_{\mathrm{mDOM}}}{\eta_{\mathrm{pDOM}}}$ is plotted over the muon energy (Fig. 6.8).

In the left plot, there is no clear dependency recognizable. The ratio fluctuates around 1.03. In contrast to that, with veto region `1_15` and strategy `first_half` the ratio starts with about 1.2 for 400 GeV and decreases with rising energy towards 1. The reason for this is, that at around 50 TeV this veto definition approaches the maximum as previous plots reveal.

At high energies, veto efficiencies converge to 100 % and the absolute difference between η_{mDOM} and η_{pDOM} shrinks. In this range, the ratio between the passing fractions becomes important. For example, a pDOM yielding $\eta_{\mathrm{pDOM}} = 98$ % confronted with a mDOM vetoing 99 % in the same energy bin implies the mDOM to have only half the passing rate of the pDOM. The fraction $\frac{1-\eta_{\mathrm{mDOM}}}{1-\eta_{\mathrm{pDOM}}}$ is plotted over muon energy for the same veto definitions as previously, to show the passing rate ratio (Fig. 6.9).

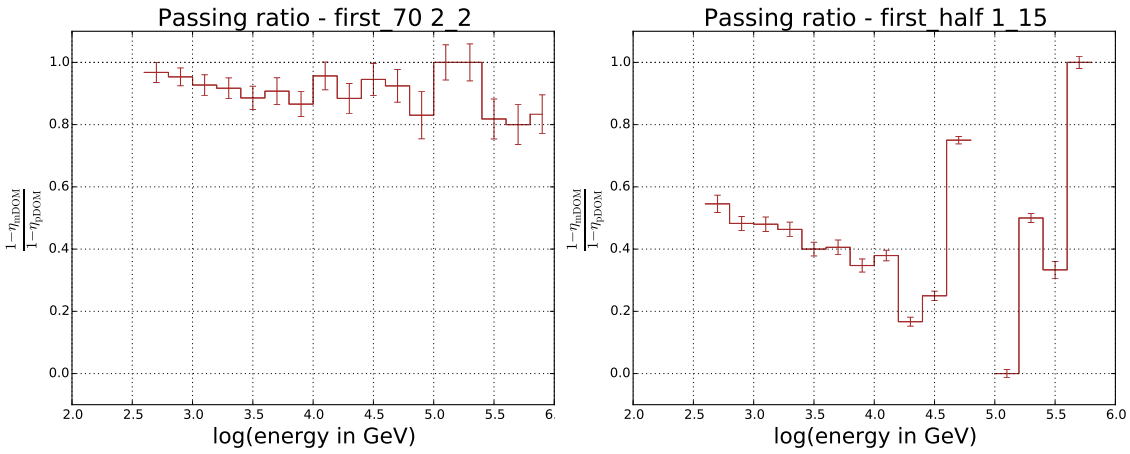

Figure 6.9: The ratio $\frac{1-\eta_{\mathrm{mDOM}}}{1-\eta_{\mathrm{pDOM}}}$. *Left:* For the veto definition `first_70/2_2`. *Right:* The veto combination `first_half/1_15`.

For $\eta_{\mathrm{pDOM}} = \eta_{\mathrm{mDOM}}$ the value is 1, except for $\eta_{\mathrm{pDOM}} = \eta_{\mathrm{mDOM}} = 100$ % where it is not defined. A fraction less than 1 corresponds to a more efficient mDOM and vice versa. For both veto combinations $\frac{1-\eta_{\mathrm{mDOM}}}{1-\eta_{\mathrm{pDOM}}} \leq 1$ and decreases further with higher energy. Above $\sim$ 100 TeV statistical fluctuations are dominating. At about 1 TeV/10 TeV/100 TeV the veto definition using region `2_2` achieves passing rates of approximately $0.93 \pm 0.04/0.96 \pm 0.05/1.00 \pm 0.06$. In the same energy bins, the `first_half/1_15` combination leads to $0.480 \pm 0.024/0.379 \pm 0.017/0.000 \pm 0.014$. The values above $\sim 10^{4.5}$ GeV are dominated by statistical fluctuations, so they are not meaningful within their error. The left plot in Fig. 6.9 shows a falling progress, but this is not reflected by the chosen energy bins. Via extrapolation by eye one finds rather $\frac{1-\eta_{\mathrm{mDOM}}}{1-\eta_{\mathrm{pDOM}}}|_{\texttt{first\_70/2\_2}} \approx 0.85$ and $\frac{1-\eta_{\mathrm{mDOM}}}{1-\eta_{\mathrm{pDOM}}}|_{\texttt{first\_half/1\_15}} \approx 0.18$.
The plots referring to the remaining 14 veto definitions are arranged in the appendix (Fig. A.10 - A.13).

6.2.1.4. Angular Dependencies

The muon energy is not the only quantity, which the veto efficiency depends on. Due to the irregular Sunflower geometry, η varies with the incident angle of the particle. As discussed in section 6.1, the azimuth distribution of muon events fluctuates. Comparing the veto efficiency separately for certain azimuth ranges would not yield useful information since the differences were in the same order as the fluctuations. Possibly, with a fine azimuthal binning, a distinct dependency could be observed, however, this would require a lot more statistics than available for this study.

In contrast, a strong dependency on the zenith angle is expected, caused by the different vertical and horizontal spacings. To illustrate that, the veto efficiency is plotted over $\cos(\theta)$

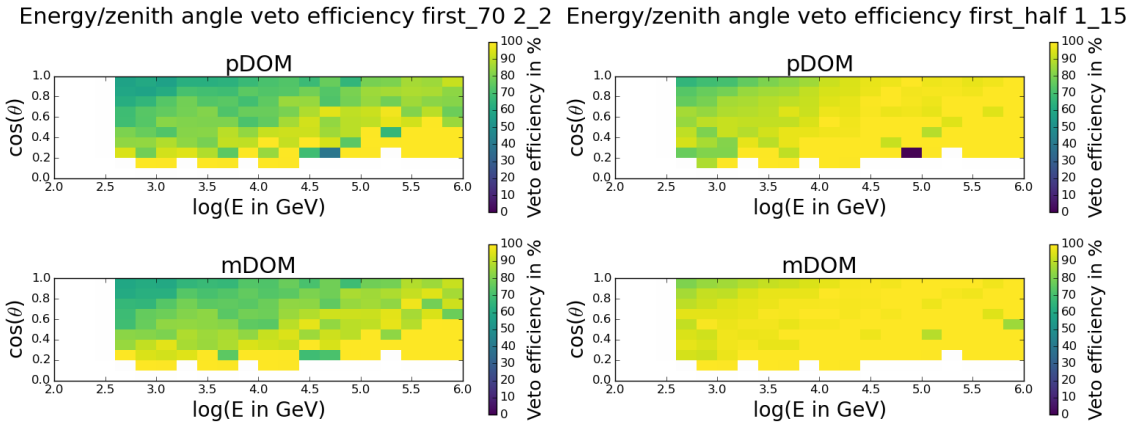

Figure 6.10: The veto efficiency binned 2-dimensional over the cosine of zenith and Monte Carlo muon energy. *Left:* Using `first_70` and `2_2`. *Right:* With combination `first_half/1_15`.

and energy, choosing again the veto definitions `first_70/2_2` and `first_half/1_15` (Fig. 6.10). In order to survey the whole zenith range until the horizon, the zenith cut is omitted here. The track length cut on 1 600 m is retained and indirectly results in an energy cut for low E_μ.

This comparison, again, confirms the increased veto efficiency of the mDOM with respect to the pDOM. The growing η with energy gets affirmed, as well. Additionally, a definite dependency on the zenith angle is revealed. For a given muon energy, horizontal events are more likely to be detected as incoming tracks. From the viewpoint of an vertically down-going track, the also vertically deployed strings allow relatively large spaces where muons can sneak through into the fiducial volume. From the side view, the 17 m vertical spacing as well as the irregular Fermat geometry provide a more reliable veto hull. The outliers, like the 0 % bin in the top right plot, are credited to reduced statistics for high energies and zenith angle.

6.2.1.5. Extrapolation in Energy

The simulated datasets `20115` and `20134` range to a maximum energy value of ~ 20 TeV and 1 PeV, respectively. One approach to estimate the veto efficiency for atmospheric muons with higher energy is to extrapolate the passing fraction $1 - \eta$. Both chosen plots veto definions `first_70/2_2` and `first_half/1_15` are shown in Fig. 6.11.

The progress of $\log(1-\eta)$ is curved up to TeV energies. Beyond that it nearly resembles a linear behavior. The errorbars grow with increasing energy due to the few events. For both veto definitions, a linear fit is adapted to the course of $\log(1-\eta_{\mathrm{pDOM}})$ and $\log(1-\eta_{\mathrm{mDOM}})$, respectively. Following an estimation by eye, the fit ranges from $10^{3.5}$ GeV to 10^{6} GeV.

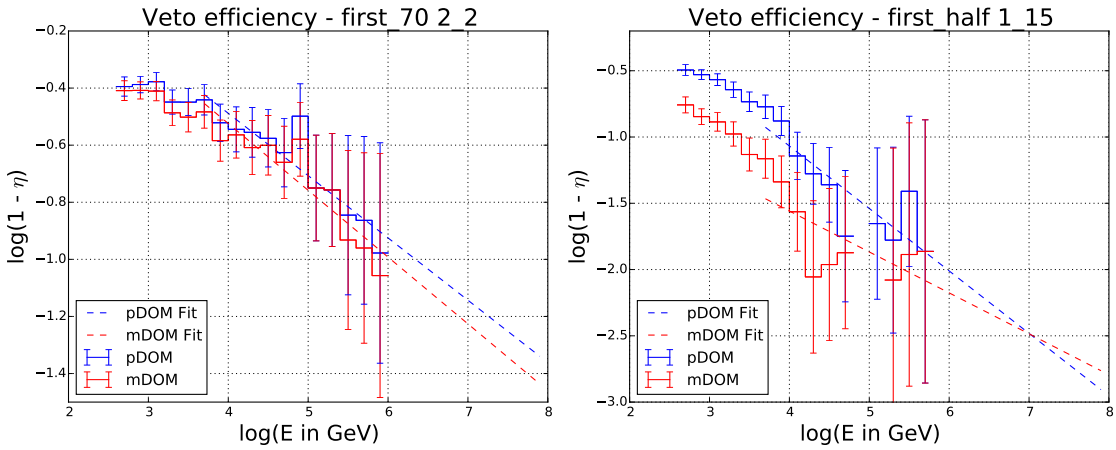

Figure 6.11: $\log(1-\eta)$ plotted over muon energy with linear Fit. *Left:* Using the veto definition `first_70/2_2`. *Right:* Combining region `1_15` with strategy `first_half`.

	`first_70` & `2_2`		`first_half` & `1_15`	
	a	b	a	b
pDOM	-0.218	0.385	-0.471	0.817
mDOM	-0.234	0.412	-0.309	0.323

Table 4: Fit parameters for the two veto strategies shown in Fig. 6.11, and for pDOM and mDOM, respectively.

The parameters obtained by a fix $a \cdot \log(E) + b$ fit function are listed in Tab. 4 and can be plugged in

$$\eta = 1 - \left(\frac{E}{\text{GeV}}\right)^{a} \cdot 10^{b}$$

to calculate an estimate for the veto efficiency.
The crossing of the fit lines in the right plot in Fig. 6.11 is not expected since it implies greater η_{pDOM} with respect to the mDOM for high energies. This behavior can be caused by the strong fluctuations above 100 TeV. Some values for η are calculated for the fit on the `first_70/2_2` veto combination (Tab. 5).

η	10^4 GeV	10^6 GeV	10^8 GeV
pDOM	67.4 %	88.1 %	95.6 %
mDOM	70.1 %	89.8 %	96.5 %

Table 5: Calculated values for η_{pDOM} and η_{mDOM}, respectively. Energy values inside and beyond the simulated range are chosen.

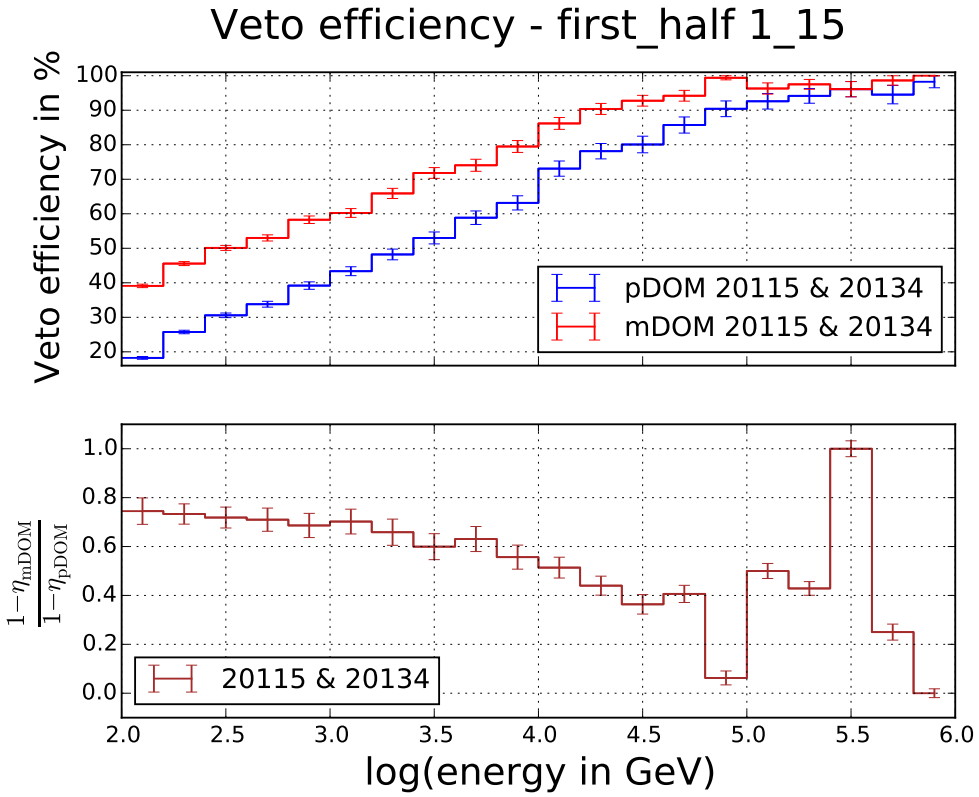

Figure 6.12: *Top:* The veto efficiency for the pDOM and mDOM with requiring at least four veto hits. *Bottom:* The respective passing ratio.

6.2.1.6. Demand for More Veto Hits

Photomultiplier noise is not included in this study, however, in reality the spontaneous triggering of a veto DOM can have an effect on the veto efficiency. The required number of veto hits (satisfying regional and temporal restrictions) per event is raised to four in order to observe the influence of the demanded veto hit number. The veto efficiencies and the passing ratio are plotted for the `first_half/1_15` veto definition in Fig. 6.12.

Once more, the mDOM achieves higher veto efficiency. The total values are distinctly lower (approx. 39.2 % (pDOM)/58.3 % (mDOM) versus 70.5 %/85.8 % at around 1 TeV for one required veto hit (cf. Fig. 6.7)). The passing ratio is higher than for one veto hit, meaning the mDOM is working less effective compared to the pDOM. By demanding for four veto hits, just below 1 TeV $\frac{1-\eta_{\mathrm{mDOM}}}{1-\eta_{\mathrm{pDOM}}} = 0.69 \pm 0.05$ (versus $\frac{1-\eta_{\mathrm{mDOM}}}{1-\eta_{\mathrm{pDOM}}}|_{1\text{ hit}} = 0.482 \pm 0.022$). With $E_\mu \gtrsim$10 TeV it still increases from 0.379 ± 0.017 to 0.51 ± 0.05.

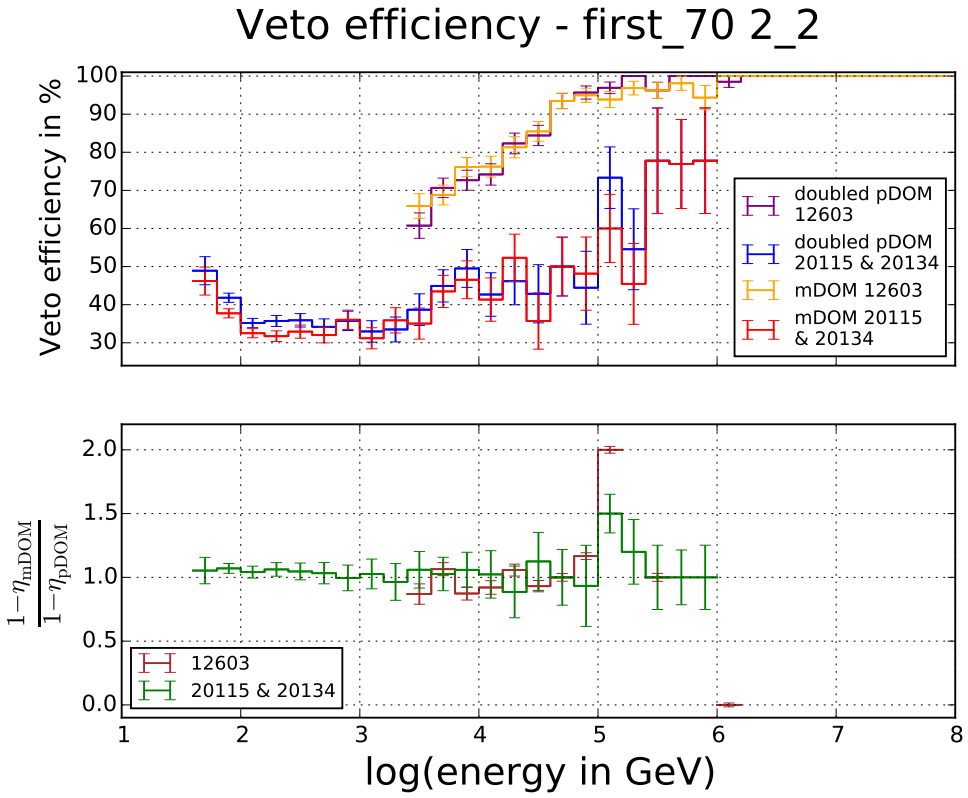

Figure 6.13: *Top:* The veto efficiency using the veto `first_70/2_2`. Old and new datasets are split. *Bottom:* The respective ratio $\frac{1-\eta_{\mathrm{mDOM}}}{1-\eta_{\mathrm{pDOM}}}$. For low energies the pDOM QE is scaled with 2.24 (green), for high-energetic muons with the factor 2 (brown) (cf. Tab. 2).

6.2.2. pDOM/mDOM Comparison Using Equal Sensitive Area

All three datasets can be merged in order to investigate the solitary effect of the mDOM design. Therefore, set `12603` with the 2×scaled pDOM QE and the new sets `20115` and `20134` with the 2.24×QE are combined. As previously described, the energy values of the new datasets are corrected to compensate the 150 m difference in starting point distance. Owing to the deviating zenith distribution, only events satisfying $\cos(\theta) > 0.95$ are considered. Additionally to the 1 600 m length cut, the start point of the kept muon tracks has to lie at least 300 m insider the Gen2 footprint. Those three cuts aim to avoid corner clippers and leave events penetrating IceCube from above and for a long distance. Selected analyses from section 6.2.1 are redone with equalized sensitive PMT area.

Like before, for the veto combinations `first_70/2_2` and `first_half/1_15` the veto efficiency is plotted over the muon energy (Fig. 6.13 and 6.14).
Considering datasets `20115` and `20134` first, with the `2_2` region the veto efficiencies are

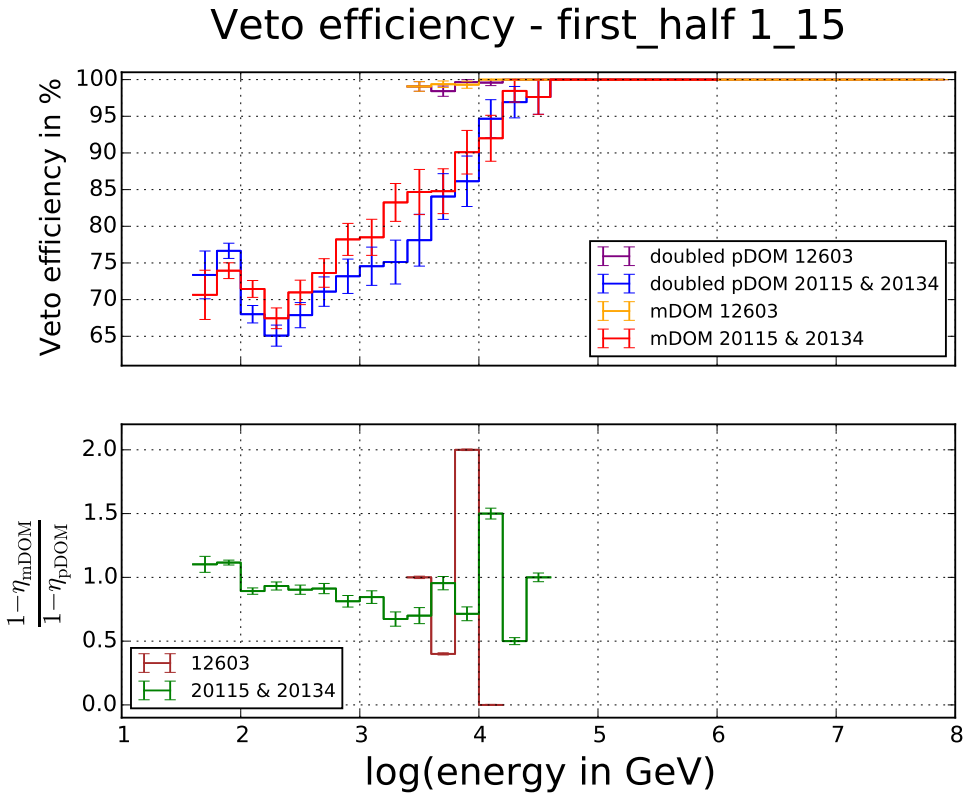

Figure 6.14: *Top:* The veto efficiency using the veto `first_half/1_15`. Old and new datasets are split. *Bottom:* The respective ratio $\frac{1-\eta_{\mathrm{mDOM}}}{1-\eta_{\mathrm{pDOM}}}$. For low energies the pDOM QE is scaled with 2.24 (green), for high-energetic muons with the factor 2 (brown) (cf. Tab. 2).

close to each other, however, η_{pDOM} tends to exceed mostly as the ratio curve below illustrates ($\frac{1-\eta_{\mathrm{mDOM}}}{1-\eta_{\mathrm{pDOM}}} > 1$). Using the `1_15` veto region, the mDOM provides better veto efficiency, except for low energies. Here, for both vetos the effect of again increasing veto efficiency with decreasing muon energy emerges. This can be explained by the overestimation of low-energetic events as mentioned in section 6.2. The ratio $\frac{1-\eta_{\mathrm{mDOM}}}{1-\eta_{\mathrm{pDOM}}}$ descends using region `1_15`.

The veto efficiencies obtained by set `12603` are significantly higher. This behavior should be avoided by the cuts (down-going, long track and start within narrowed footprint) to obtain highly comparable events from all datasets. However, the events in the high-energy dataset (`12603`) tend to produce more hits in the veto than those from the new sets `20115` and `20134` under supposedly same conditions. This deviating veto response is confirmed by regarding exemplary Monte Carlo muon tracks from all sets with the event viewer 'steamshovel'. Changes in the simulation software during the nine months between the simulations of new and old datasets might be responsible for the different results for η.

7. Conclusion

In this thesis both DOM designs for IceCube-Gen2, the pDOM and the mDOM, were compared in terms of their veto capability. Angular and energetic dependencies were identified and the influence of several details of the veto definition were investigated.

The efficiency in vetoing atmospheric muons is clearly growing with the muon's energy. The direct comparison of veto regions revealed the setup with one vertical and 15 horizontal layers as most efficient. The effects of the strategy choice was less significant. However, considering high-energetic muons, using the first temporal half of each event resulted in the lowest passing rates. Additionally, the veto efficiency decreases with the zenith angle owing to the asymmetric detector geometry of Gen2. Demanding for more than one veto hit might reduce the negative influence of PMT noise, but it also reduced the veto efficiency advantage of the mDOM distinctly.
Applying the realistic PMT quantum efficiencies, the mDOM consistently exceeded the pDOM in terms of vetoing atmospheric muons within the estimated errors. The veto definition that emerged as most effective, yielded a passing ratio mDOM:pDOM of 0.480, 0.379 and 0.18 for the energies 1 TeV, 10 TeV and 100 TeV, respectively. The absolute veto efficiencies above 10 TeV/100 TeV arose as 92.8 %/97.8 % for the pDOM and 97.3 %/100 % for the mDOM. The demand for four veto hits, instead of one, as veto condition lead to a passing ratio implying a less efficient mDOM ($0.482 \rightarrow 0.69$ just below 1 TeV and $0.379 \rightarrow 0.51$ at about 10 TeV). With increasing muon energy large uncertainties on the veto efficiency and thereof derived quantities emerged.
Not all datasets used in this study were compatible. Cuts were applied, to enforce the same conditions for track events, and energy losses were approximated to compensate the different starting positions. Nevertheless, the deviating veto hit responses lead to divergent results. Hence, a combined analysis with larger energy range and higher statistics was not feasible.

For future analyses, larger consistent datasets are necessary. It will also be important to quantify the effect of a larger veto on the neutrino signal efficiency. Neutrino induced track event should preferably not be discarded as atmospheric background. Therefore, a combined simulation of neutrino interactions in and around IceCube as well as atmospheric background can lead to an optimized definition of veto criteria.
In order to evaluate the justification of researching new DOM types and detector geometries, the quantities obtained in this study might be scaled with the estimated cost per DOM or string.

A. Appendix

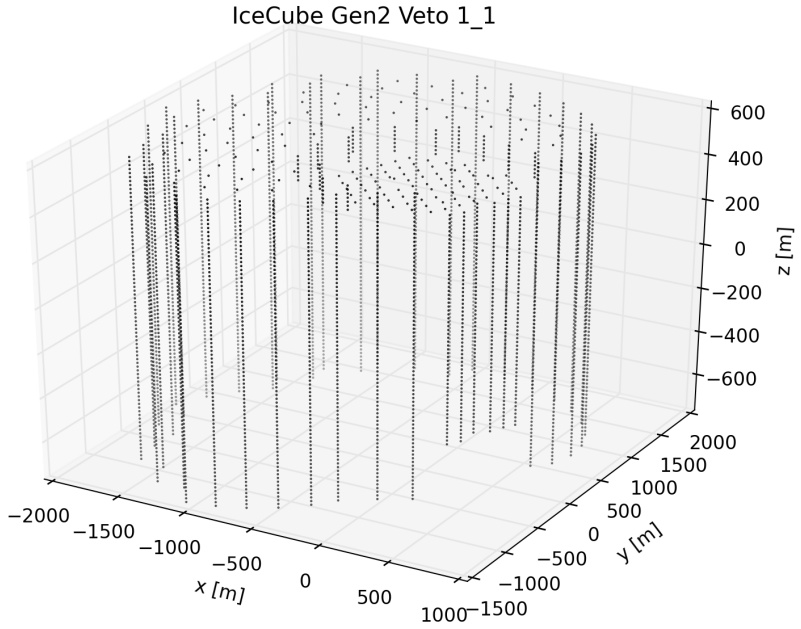

Figure A.1: The veto DOMs of region `1_1`, each represented by one dot; the point $(0, 0, 0)$ denotes the center of IC-86.

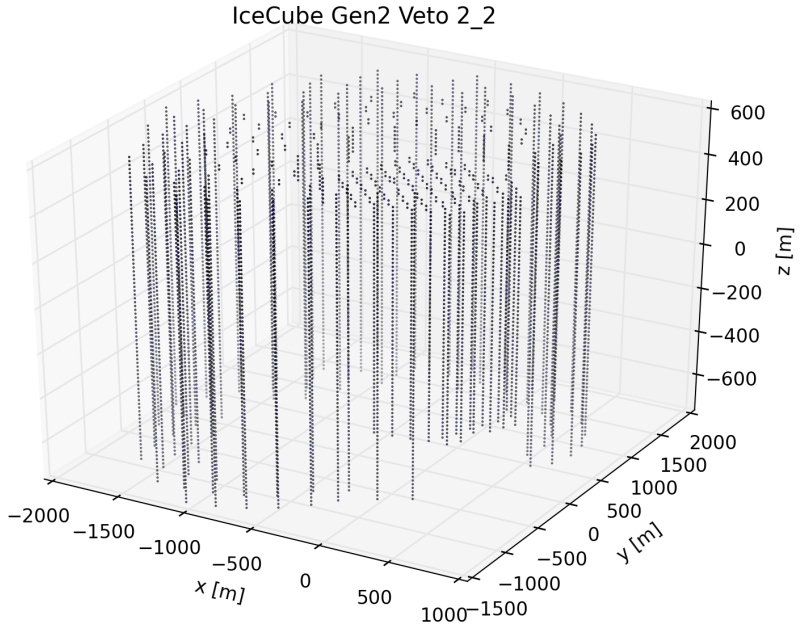

Figure A.2: The veto DOMs of region 2_2, each represented by one dot; the point $(0, 0, 0)$ denotes the center of IC-86.

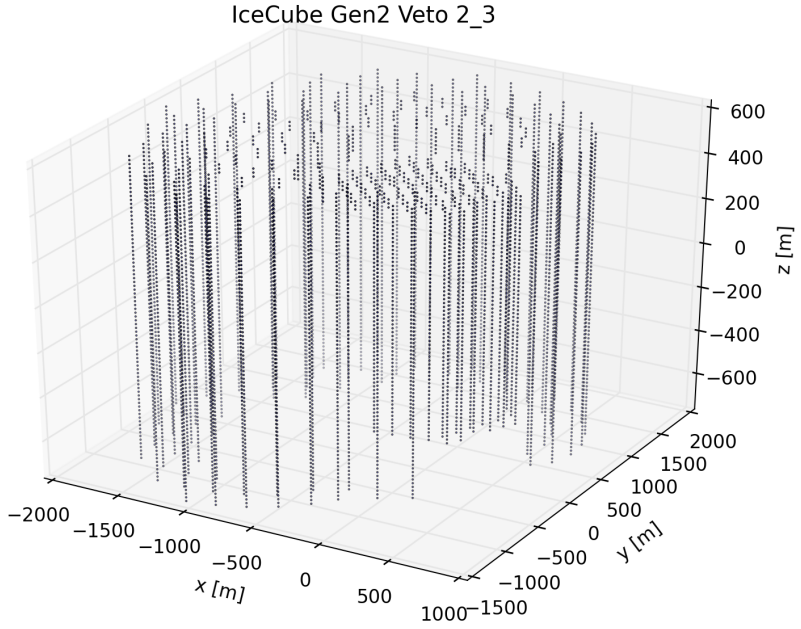

Figure A.3: The veto DOMs of region 2_3, each represented by one dot; the point $(0, 0, 0)$ denotes the center of IC-86.

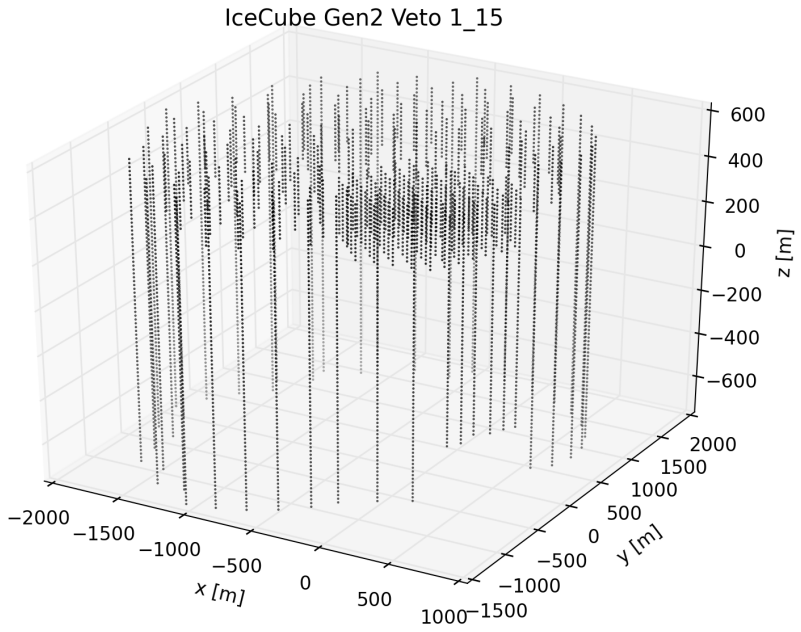

Figure A.4: The veto DOMs of region `1_15`, each represented by one dot; the point $(0, 0, 0)$ denotes the center of IC-86.

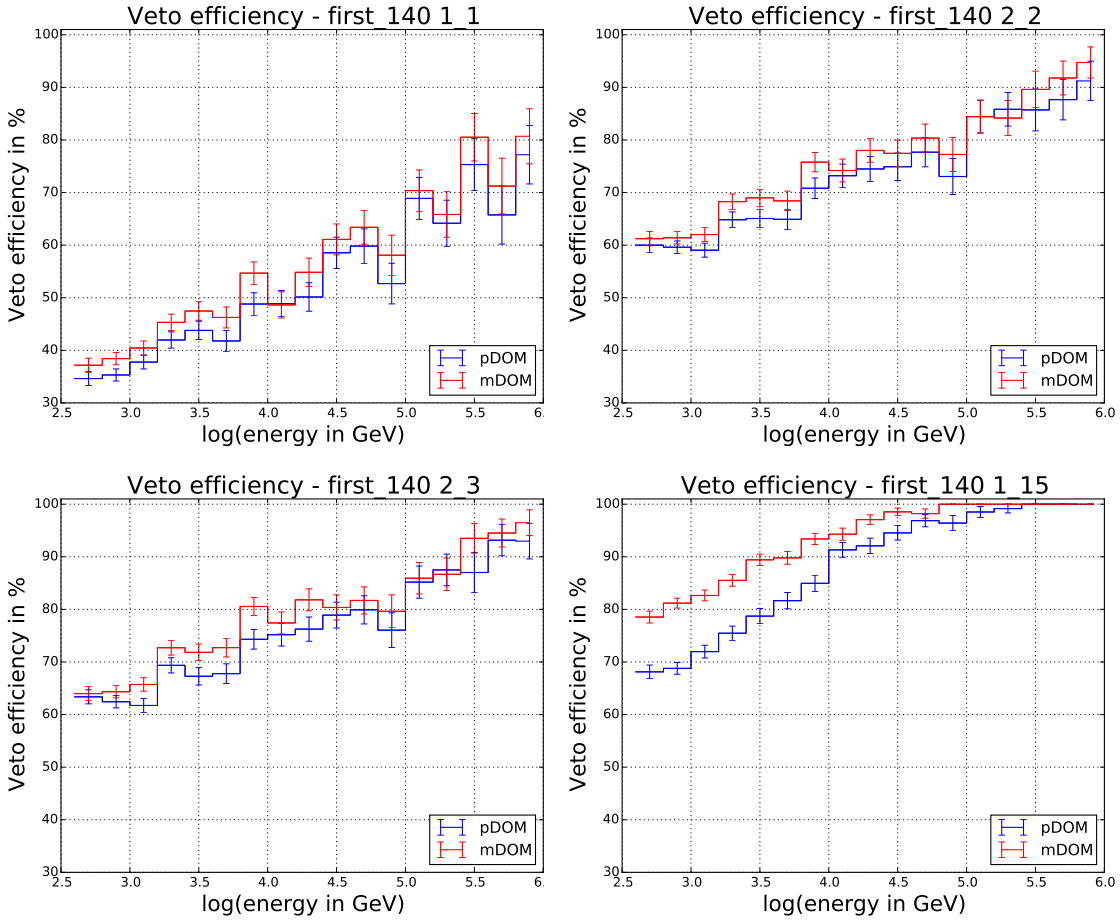

Figure A.5: Confrontation of the veto efficiencies in all four regions using veto strategy `first_140`.

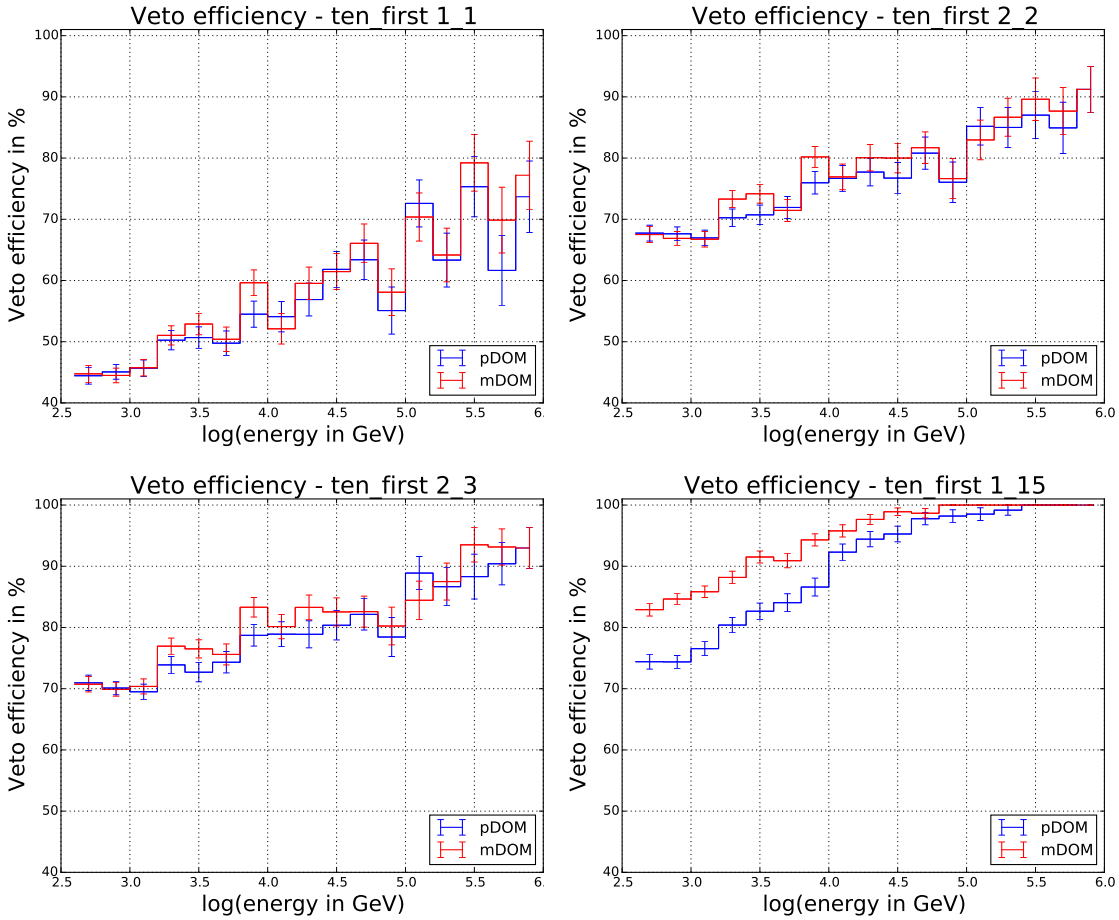

Figure A.6: Confrontation of the veto efficiencies in all four regions using veto strategy `ten_first`.

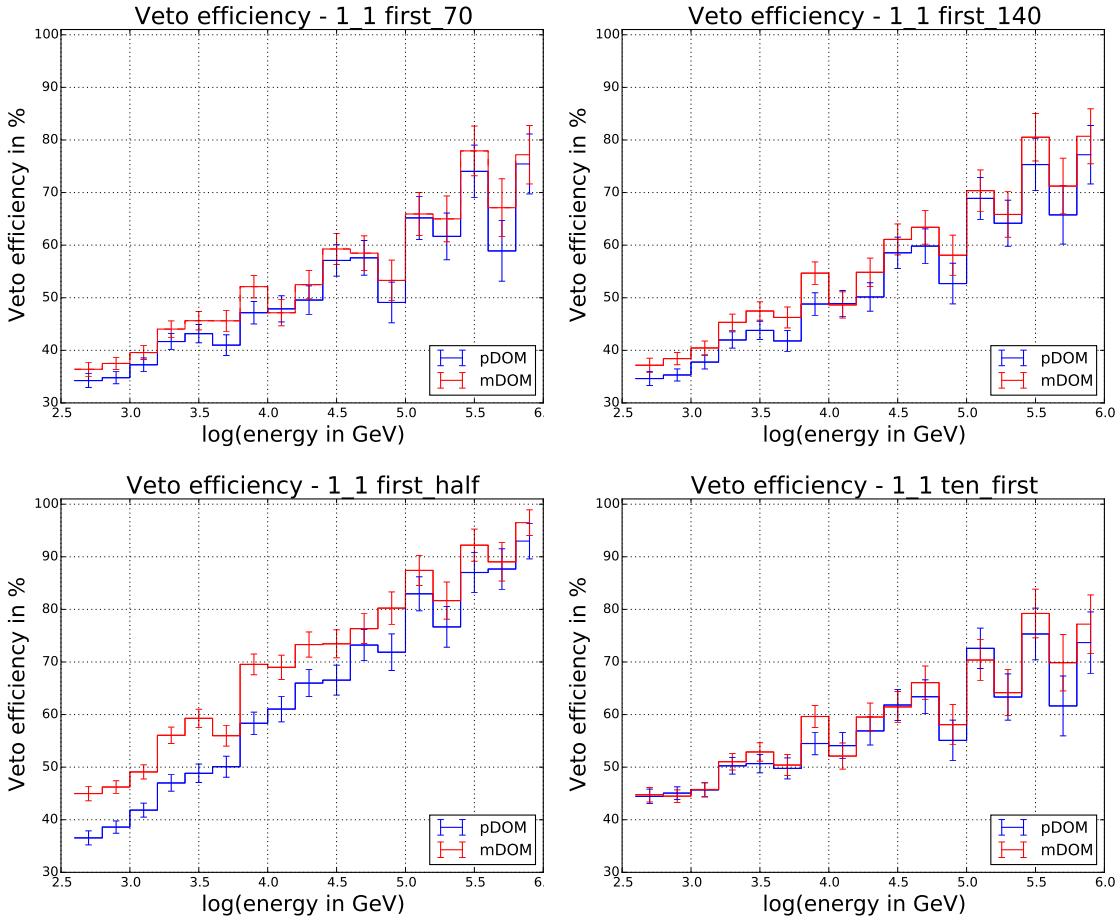

Figure A.7: Confrontation of the veto efficiencies with all four strategies in veto region 1_1.

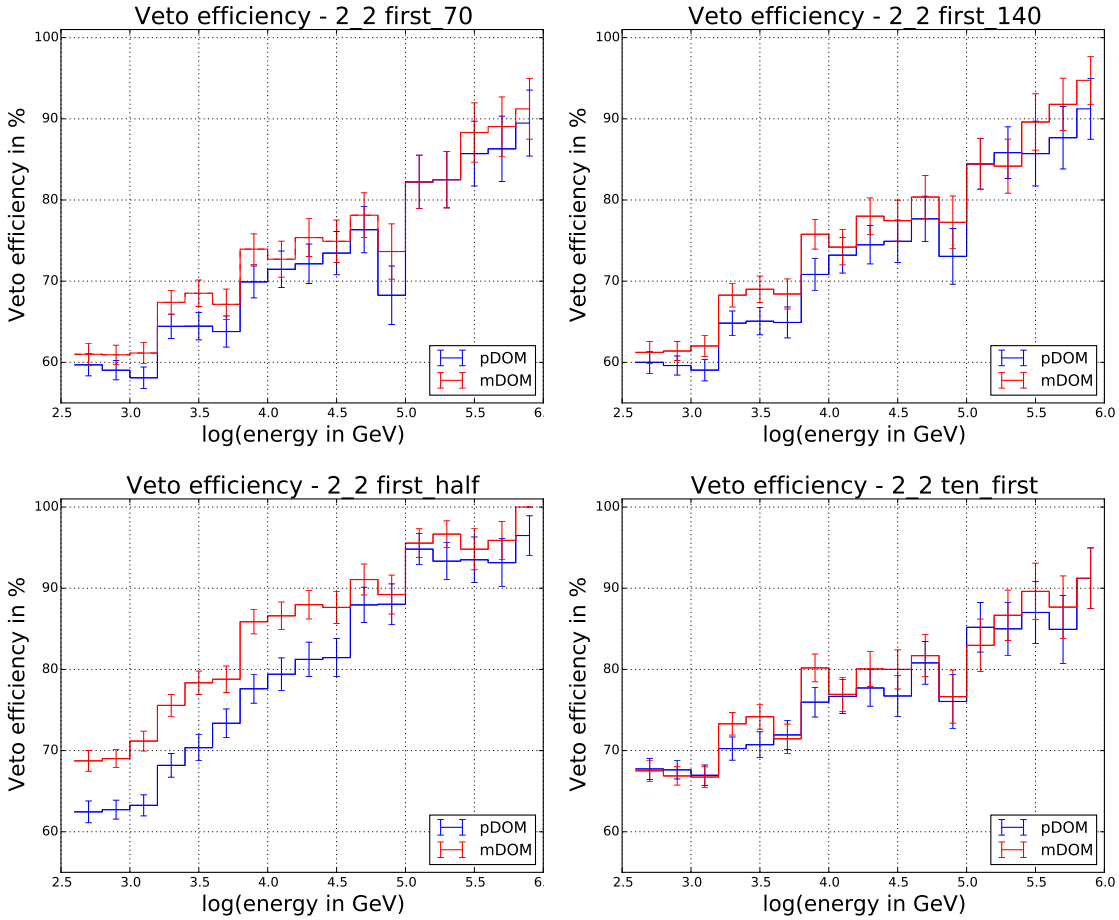

Figure A.8: Confrontation of the veto efficiencies with all four strategies in veto region 2_2.

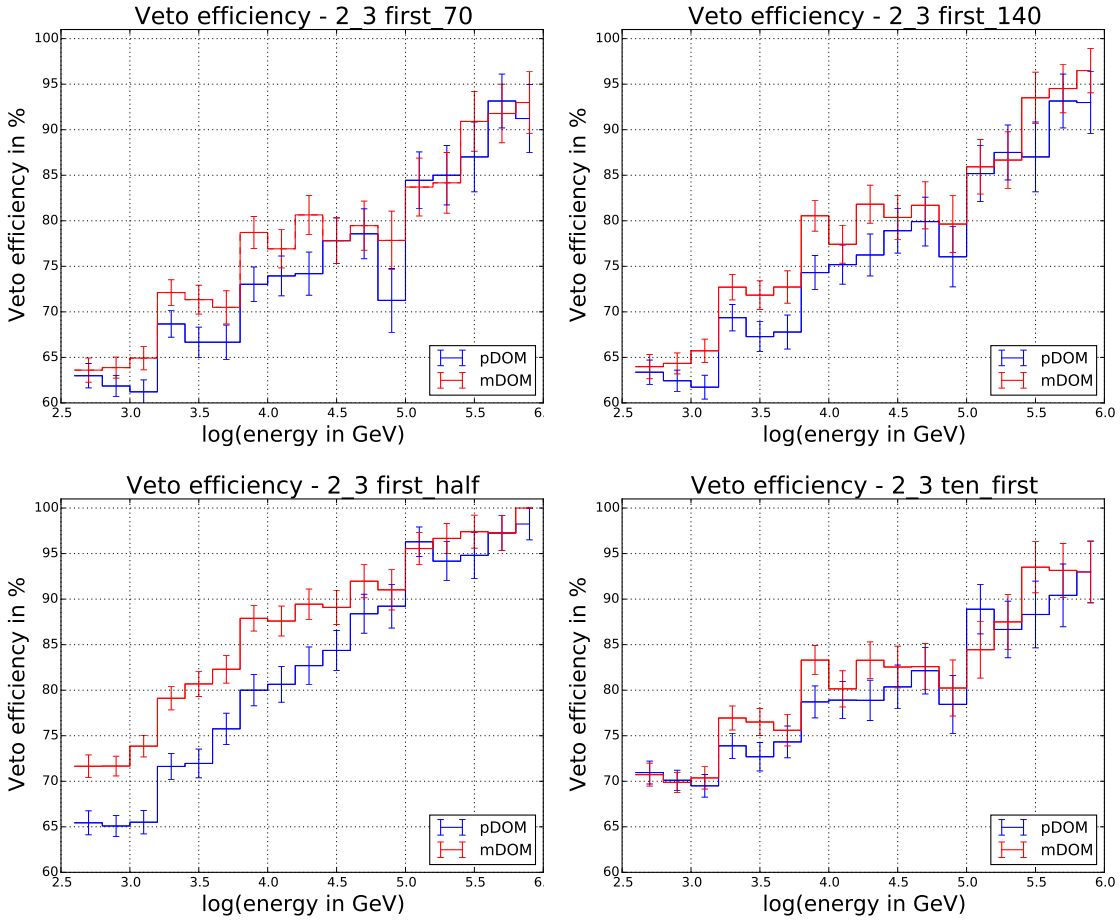

Figure A.9: Confrontation of the veto efficiencies with all four strategies in veto region 2_3.

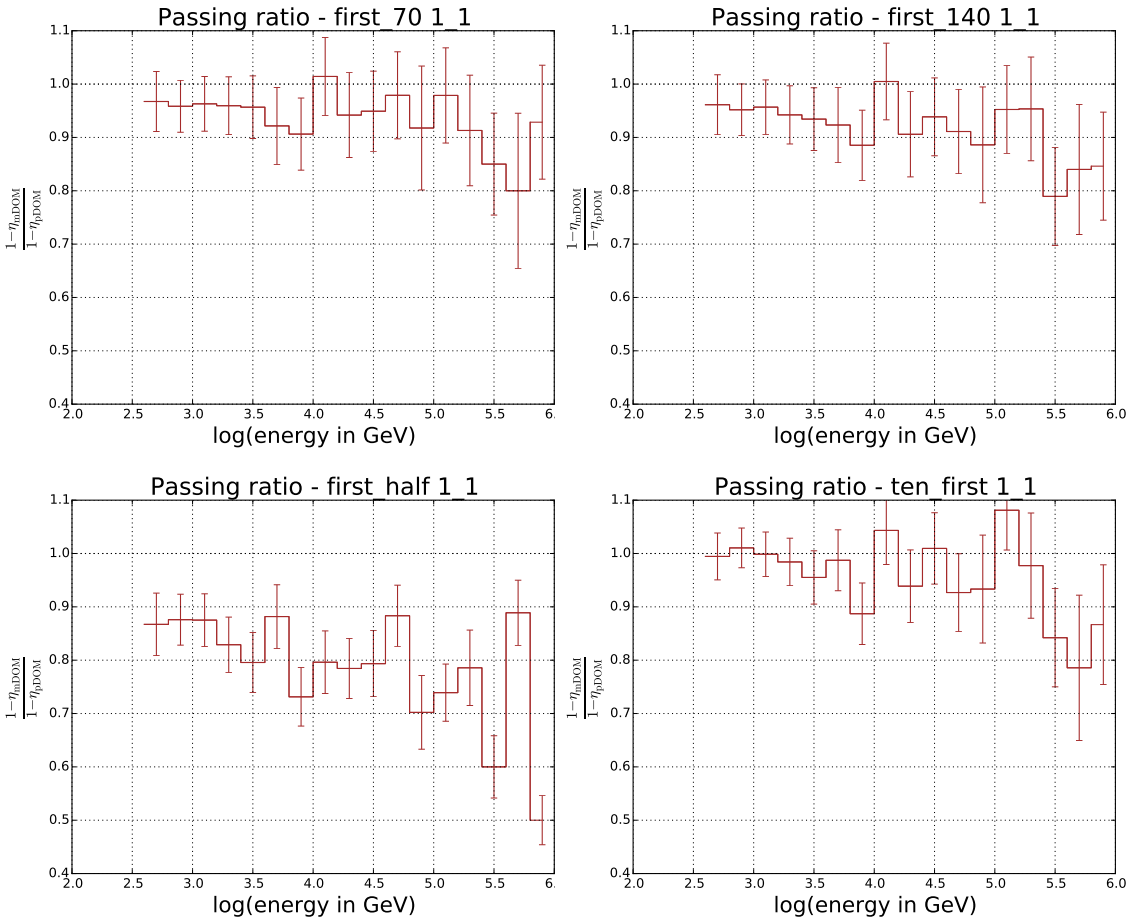

Figure A.10: Confrontation of the ratio $\frac{1-\eta_{\mathrm{mDOM}}}{1-\eta_{\mathrm{pDOM}}}$ with all four strategies in veto region 1_1.

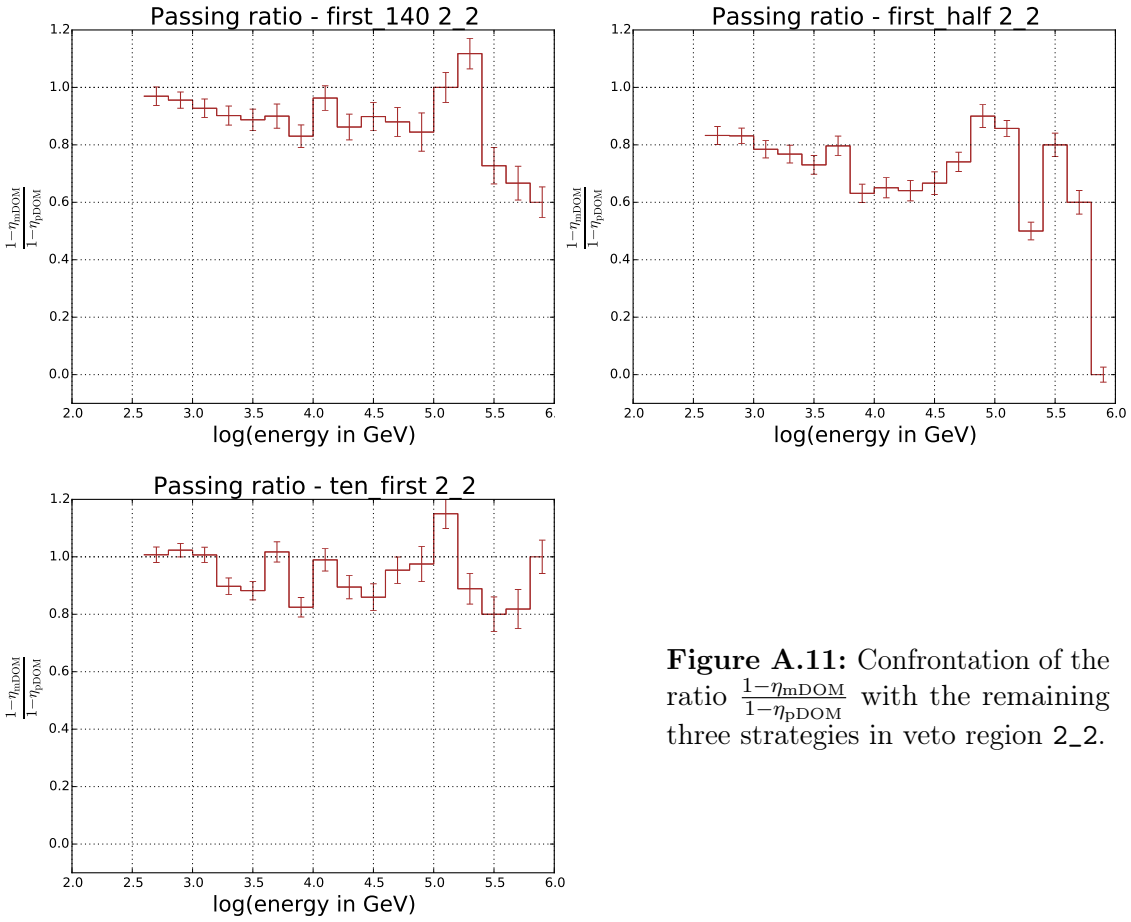

Figure A.11: Confrontation of the ratio $\frac{1-\eta_{\mathrm{mDOM}}}{1-\eta_{\mathrm{pDOM}}}$ with the remaining three strategies in veto region 2_2.

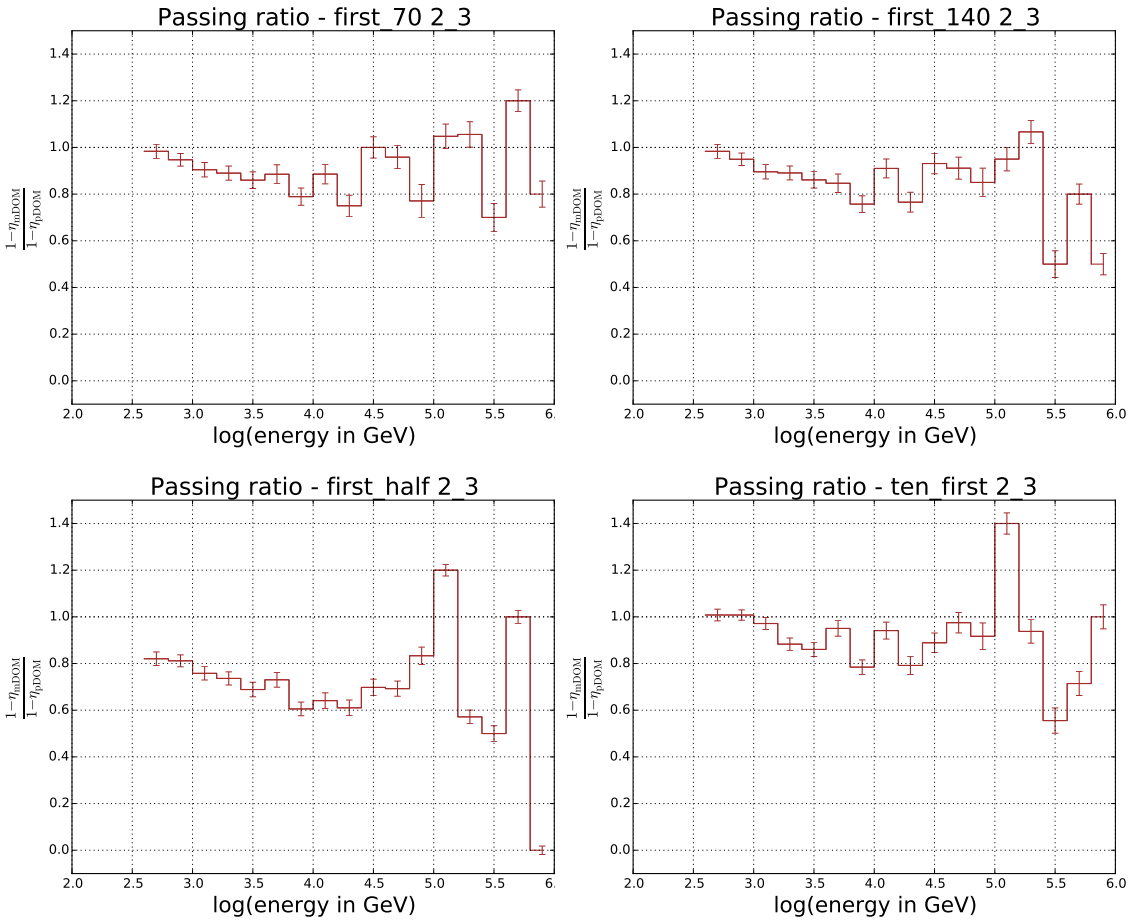

Figure A.12: Confrontation of the ratio $\frac{1-\eta_{\mathrm{mDOM}}}{1-\eta_{\mathrm{pDOM}}}$ with all four strategies in veto region 2_3.

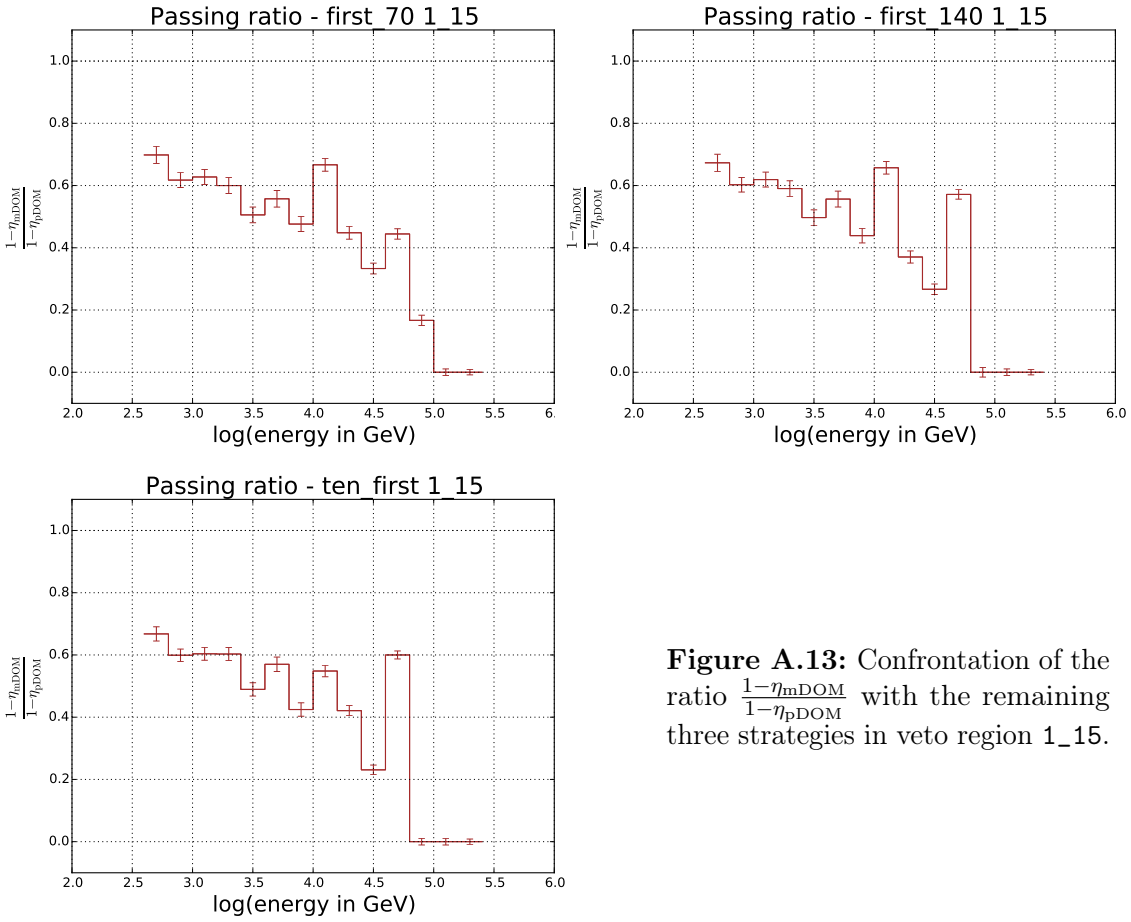

Figure A.13: Confrontation of the ratio $\frac{1-\eta_{\mathrm{mDOM}}}{1-\eta_{\mathrm{pDOM}}}$ with the remaining three strategies in veto region 1_15.

References

[1] IceCube Science. http://icecube.wisc.edu/science. accessed August 2017.

[2] IceCube Science - Detector. http://icecube.wisc.edu/science/icecube/detector. accessed August 2017.

[3] IceCube Science - IceTop. https://icecube.wisc.edu/science/icetop/. accessed August 2017.

[4] IceCube Software Documentation - MuonGun. http://software.icecube.wisc.edu/documentation/projects/MuonGun/index.html. accessed August 2017.

[5] WIPAC NEWS - Everything you always wanted to know about the IceCube detector. https://wipac.wisc.edu/news/article/everything-you-always-wanted-know-about-icecube-detector. accessed August 2017.

[6] M. G. Aartsen et al. (IceCube Collaboration) Evidence for High-Energy Extraterrestrial Neutrinos at the IceCube Detector. *Science*, 342(6161), 2013.

[7] M. G. Aartsen et al. (IceCube Collaboration) First observation of PeV-energy neutrinos with IceCube. *Physical review letters*, 111(2), 2013.

[8] M. G. Aartsen et al. (IceCube Collaboration) Energy Reconstruction Methods in the IceCube Neutrino Telescope. *Journal of Instrumentation*, 9(3), 2014.

[9] M. G. Aartsen et al. (IceCube Collaboration) Observation of High-Energy Astrophysical Neutrinos in Three Years of IceCube Data. *Physical review letters*, 113(10), 2014.

[10] M. G. Aartsen et al. (IceCube-Gen2 Collaboration) IceCube-Gen2: A Vision for the Future of Neutrino Astronomy in Antarctica. *arXiv:1412.5106*, 2014.

[11] M. G. Aartsen et al. (IceCube PINGU Collaboration) Letter of Intent: The Precision IceCube New Generation Upgrade (PINGU). *arXiv:1401.2046*, 2014.

[12] M. G. Aartsen et al. (IceCube Collaboration) Atmospheric and Astrophysical Neutrinos above 1 TeV Interacting in IceCube. *Physical Review D*, 91(2), 2015.

[13] R. Abbasi et al. (IceCube Collaboration) The Design and Performance of IceCube DeepCore. *Astroparticle physics*, 35(10), 2012.

[14] A. Bhattacharya et al. The Glashow resonance at IceCube: signatures, event rates and pp vs. $p\gamma$ interactions. *Journal of Cosmology and Astroparticle Physics*, 2011(10), 2011.

[15] E. Blaufuss, C. Kopper, and C. Haack. (IceCube Collaboration) The IceCube-Gen2 High Energy Array. *PoS(ICRC2015)1146*, 2015.

[16] L. Classen and A. Kappes. (IceCube-Gen2 Collaboration) Multi-PMT optical modules for IceCube-Gen2. *PoS(ICRC2015)1147*, 2015.

[17] P. Coppin. InIce veto studies for the future IceCube-GEN2 neutrino observatory, 2017.

[18] P. Coppin, S. Toscano, and J. Lünemann. (IceCube-Gen2 Collaboration) In-ice self-veto techniques for IceCube-Gen2. *PoS(ICRC2017)945*, 2017.

[19] J. Dumm. IceCube Overview. 2016.

[20] M. A. DuVernois et al. (IceCube-Gen2 Collaboration) The IceCube Generation-2 Digital Optical Module and Data Acquisition System. *PoS(ICRC2015)1148*, 2015.

[21] T. K. Gaisser et al. A generalized self-veto probability for atmospheric neutrinos. *Physical Review D*, 90(2), 2014.

[22] D. Hebecker et al. A Wavelength-shifting Optical Module (WOM) for in-ice neutrino detectors. *EPJ Web of Conferences*, 116:01006, 2016.

[23] H. Ijiri. (IceCube-Gen2 Collaboration) A dual-PMT optical module (D-Egg) for IceCube-Gen2. *PoS(ICRC2015)1137*, 2015.

[24] U. Katz and C. Spiering. High-Energy Neutrino Astrophysics: Status and Perspectives. *Progress in Particle and Nuclear Physics*, 67(3), 2011.

[25] T. Kittler. Reconstruction and simulation with multi PMT optical modules for IceCube-Gen2. 2016.

[26] C. Kopper, W. Giang, and N. Kurahashi. (IceCube Collaboration) Observation of Astrophysical Neutrinos in Four Years of IceCube Data. *PoS(ICRC2015)1081*, 2015.

[27] P. Pfeiffer. New optical sensors for IceCube-Gen2. 2016.

[28] L. Rädel and C. Wiebusch. Calculation of the Cherenkov light yield from low energetic secondary particles accompanying high-energy muons in ice and water with Geant4 simulations. *Astroparticle Physics*, 38, 2012.

[29] S. Schönert et al. Vetoing atmospheric neutrinos in a high energy neutrino telescope. *Physical Review D*, 79(4), 2009.

[30] A. Schönwald, A. M. Brown, and L. Mohrmann. (IceCube Collaboration) Search for diffuse astrophysical neutrinos with cascade events in the IceCube-59 detector. *arXiv:1309.7003*, 2013.

[31] C. Spiering. Towards High-Energy Neutrino Astronomy. A historical review. *The European Physical Journal H*, 37(3), 2012.

[32] S. Toscano. Highlights from IceCube. 2016.

[33] J. van Santen. (IceCube-Gen2 Collaboration) IceCube-Gen2: the next-generation neutrino observatory for the South Pole. *PoS(ICRC2017)991*, 2017.

Acknowledgement

Finally, I hereby want to thank all people who enabled me to write and helped working on this thesis. First of all, thanks to Prof. Gisela Anton and Thorsten Glüsenkamp for coming up with this deeply interesting topic and allowing me to participate in the IceCube Fall Collaboration Meeting.

A huge thank you to the IceCube group at ECAP and Thomas Kittler in particular for his multiple advices concerning advanced scientific programming.

Thanks to the whole IceCube Collaboration for providing helpful information and tips, whenever a script does not what it is supposed to do. Worth pointing out especially are Jakob van Santen from DESY Zeuthen for providing useful tools for my analysis and answers concerning the simulations he submitted for me, and Paul Coppin from the Vrije Universiteit Brussel for facilitating the definition of the veto regions.

For their proofreading, I want to thank Thomas Kittler and Gerrit Wrede, also Ulrich Peeck for at least attempting.

Erklärung

Hiermit versichere ich, dass ich die vorliegende Arbeit *Muon Veto Study Comparing pDOM and mDOM for IceCube-Gen2* selbstständig verfasst und keine anderen als die angegebenen Quellen und Hilfsmittel benutzt habe, dass alle Stellen der Arbeit, die wörtlich oder sinngemäß aus anderen Quellen übernommen wurden, als solche kenntlich gemacht sind und dass die Arbeit in gleicher oder ähnlicher Form noch keiner Prüfungsbehörde vorgelegt wurde.

Unterschrift

Ort, Datum